Role of atmospheric aerosols in severe winter fog over Indo Gangetic Plains of India: a case study

Chandrakala Bharali[1], Mary Barth[2], Rajesh Kumar[2], Sachin D. Ghude[3], Vinayak Sinha[4], Baerbel Sinha[4]

[1] Dibrugarh University, Dibrugarh, Assam, India

[2] National Centre for Atmospheric Research, Boulder, CO, US

[3] Indian Institute of Tropical Meteorology, Ministry of Earth Sciences, Pune, India

[4] Department of Earth and Environmental Sciences, Indian Institute of Science Education and Research, Mohali, Punjab, India

Correspondence: chandrakalabharali@gmail.com, barthm@ucar.edu

Abstract

Winter fog and severe aerosol loading in the boundary layer over north India, especially in the Indo-Gangetic Plain (IGP), cause disruption in the daily lives of millions of people in the region. To understand better the role of atmospheric aerosols on the occurrence, spatial extent, and persistence of winter fog in the IGP, several model simulations have been performed using the Weather Research and Forecasting model coupled with chemistry (WRF-Chem). Results from WRF-Chem represented relative humidity (RH) and fog formation in agreement with observations when using the ERA-Interim reanalysis data as meteorological initial/boundary conditions and soil nudging were applied. WRF-Chem successfully simulates the spatial distribution and magnitude of $PM_{2.5}$ when evaluated with observations from the Central Pollution Control Board of India (CPCB) monitoring network. However, the aerosol composition predicted by WRF-Chem was quite different from measurements obtained during the Winter Fog Experiment (WiFEX) in Delhi, with chloride aerosol fraction being strongly underpredicted (~66.6%). By investigating a fog event on December 23-24, 2017 over central IGP, we found that the aerosol-radiation feedback weakens turbulence, lowers the boundary layer height, and increases $PM_{2.5}$ concentrations and RH within the boundary layer. The increase in RH is found to be important for fog formation and it promoted the growth of aerosol size and increased aerosol activation in the polluted environment over IGP. Loss of aerosols through deposition of cloud droplets is found to be a significant aerosol loss process during fog. The internal mixing of absorbing aerosols and hygroscopic growth reduces the single scattering albedo impacting aerosol-radiation feedbacks. Aqueous-phase chemistry increases the $PM_{2.5}$ concentrations during fog events which subsequently participates in aerosol-radiation feedback. With aerosol-radiation interaction and aqueous phase chemistry, fog formation began 1-2 hours earlier and caused a longer fog duration than when these processes were not included in the WRF-Chem simulation. These processes were also found to increase RH, stabilize the boundary layer, increase $PM_{2.5}$ promoting aerosol activation, and thus increasing the

35 fog water content over IGP. This suggests that the aerosol-radiation feedback and secondary aerosols

36 play an important role in the air quality and in the intensity and lifetime of fog over IGP.

1   Introduction

39   The Indo-Gangetic Plain (IGP; 21°35′-32°28′N latitude. and 73°50′-89°49′E longitude) in the

40 northern part of the Indian subcontinent is one of the most densely populated and heavily polluted

41 regions in South Asia. The rapid population and economic growth in the IGP region over the last decade

42 have increased air pollution over this region. This is evident from the increasing trend in AOD and NO_x

43 over India reported in recent studies (Dey and Di Girolamo, 2011; Ghude et al., 2013; Krishna Moorthy

44 et al., 2013), which has slowed and reversed only recently (Sarkar et al., 2019). The high concentration

45 of aerosols along the IGP and their adverse effects on human health and the environment are increasing

46 (Ghude et al., 2016). Consequently, more than 500 million people living in the IGP breathe air that

47 exceeds the National Ambient Air Quality (NAAQ) Standards, which has reduced the life expectancy

48 of the people (Debnath et al., 2022; Lelieveld et al., 2015). Lelieveld et al., (2015) estimated a very high

49 number of premature deaths (0.716 million per year) linked to aerosols ($PM_{2.5}$), thus making Southeast

50 Asia one of the largest regions affected by premature mortality globally.

51   One of the major environmental concerns in the IGP is the urban air quality during winter,

52 especially over the mega-cities, e.g., Delhi, located in the north-western part of IGP (Ghude et al., 2020;

53 Jena et al., 2021; Sengupta et al., 2022). Several urban air pollution hotspots along the IGP extend from

54 northwest to east with monthly average $PM_{2.5}$ greater than 200 ug m^{-3} (National Ambient Air Quality

55 Standards (NAAQS)=60 ugm^{-3}, 24 hr average) in the winter season (Bharali et al., 2019; Krishna et al.,

56 2019). IGP is dominated mainly by fine mode particulates, especially over central to eastern IGP, during

57 post-monsoon and winter (Kumar et al., 2018). Biomass burning (agricultural waste burning, domestic

58 heating, etc.) is an important contributor to the observed high $PM_{2.5}$ loading over IGP during these

59 seasons (Kulkarni et al., 2020; Pant et al., 2015; Pawar and Sinha, 2022; Sharma et al., 2010; Yadav et

60 al., 2020). Delhi is affected substantially by the emissions from agricultural waste burning in the north-

61 western states of Punjab and Haryana during the post-monsoon (October-November) season

62 (Badarinath et al., 2009; Jethva et al., 2018; Kumar et al., 2021). Studies showed that $PM_{2.5}$ increased

63 from ~50 µg m^{-3} to as high as 300 µg m^{-3} (Ojha et al., 2020), and AOD reached 0.98 with the presence

64 of absorbing aerosols (Singh et al., 2018) during the peak biomass burning in post-monsoon.

65   IGP experiences fog (both radiation and advection fog) every winter after the passage of the

66 synoptic wind system called the "Western Disturbances". The number of low visibility days due to

67 haze/fog formation has been increasing significantly (Ghude et al., 2017; Jenamani, 2007; Singh and

68 Dey, 2012), impacting socio-economic activities, e.g., aviation (Kulkarni et al., 2019). The increase in

69 the intensity and regional extent of fog over IGP is consistent with the increasing trend in aerosol

70 concentration due to increasing anthropogenic emissions (Sarkar et al., 2006; Syed et al., 2012).

71   Several factors control the formation and persistence of fog in the IGP, e.g., stable boundary
72   layer, cold temperature, availability of moisture (supplied by the Western Disturbances and irrigation
73   activities), and the aerosol number and composition (Acharja et al., 2022; Dhangar et al., 2021). It has
74   also been suggested that the atmospheric rivers (moisture incursion from Arabian Sea) act as a source
75   of water vapor over IGP, which fuels the intensification of fog and haze (Verma et al., 2022) during
76   winter. The high aerosol concentration in the boundary layer influences fog formation (Gautam et al.,
77   2007; Safai et al., 2019) over the IGP by providing the needed cloud condensation nuclei (CCN) for
78   activation into fog droplets. In addition, aerosols induce surface cooling by reducing solar radiation at
79   the surface while warming the lower troposphere by absorption (Ding et al., 2016; Yu et al., 2002). A
80   reduction in surface-reaching solar radiation by ~19% has been reported during winter over Kanpur in
81   the IGP (Dey and Tripathi, 2007). The reduced solar flux affects the boundary layer stability and depth
82   by suppressing the thermals and thus further increasing the surface aerosol concentration via aerosol-
83   radiation feedback, which is very strong over the IGP (Bharali et al., 2019). Kumar et al., (2020) have
84   shown that aerosol-radiation feedback significantly improves the accuracy of $PM_{2.5}$ and temperature
85   forecasts in Delhi. Srivastava et al., (2018) reported that the direct aerosol forcing over polluted regions
86   is very large with values up to -80.0 ± 7.2 W m^{-2} over the IGP in the winter season.

87   Aerosol-radiation interaction determines that the aerosol distribution is critical for the evolution
88   of fog (Bodaballa et al., 2022; Steeneveld et al., 2015), while microphysics is important for fog
89   formation and dispersal (Boutle et al., 2018; Maalick et al., 2016). Although the relationship between
90   the aerosol chemical composition and aerosol activation to CCN has not been fully understood yet,
91   studies have found that the chemical composition and mixing state of aerosols affect the hygroscopicity
92   (κ) of aerosols (Bodaballa et al., 2022; Ma et al., 2013; Moore et al., 2012; Zhang et al., 2014a). Fog
93   processes involve a complex interplay between local meteorology, radiation, microphysics, and aerosol
94   chemistry, making it difficult to understand the fog lifecycle (Acharja et al., 2022; Maalick et al., 2016;
95   Zhang et al., 2014b). There is considerable heterogeneity in the spatial and temporal aerosol properties
96   over IGP and the poor estimates of their mixing state. Therefore, prediction of fog by weather models
97   is still challenging with biases in fog's onset and dispersal timings.

98   Previous studies have focussed on the impacts of meteorological conditions, topography, or
99   anthropogenic emissions on the poor air quality and intensification of fog during winter over IGP (e.g.
100   Hakkim et al., 2019). However, studies on the effect of feedback induced by the aerosols on the
101   meteorological conditions and thus on aerosol concentration are very limited over this region, except
102   for a few above-mentioned studies which discuss how the aerosol-radiation feedback favors haze and
103   fog during winter. Moreover, fog can provide a medium for aqueous-phase reactions. While several
104   earlier studies have reported an increase in secondary aerosols during fog over IGP, a sensitivity study
105   examining the impact of fog on aqueous phase chemistry has not yet been done over IGP.

106   In the present work, we aim to find the suitable chemistry/physics as well as the meteorology
107   initial/boundary conditions that lead to improved simulations of fog events in the Weather Research and

108 Forecasting model coupled with chemistry (WRF-Chem; (Fast et al., 2006; Grell et al., 2005; Powers et
109 al., 2017). We also explore the role of aerosol-radiation feedback on fog properties as the high aerosol
110 loadings in northern India can impact the heating rates, temperature inversions, and boundary layer
111 height. The role of aqueous chemistry on fog properties and vice-versa is also investigated.

2 Methodology

113 Fig. 1 shows the IGP study region for the simulations. Fog occurred on both 23rd and 24th
114 December 2017 (Fig. 1a, b). The fog region is located over an area with high PM$_{2.5}$ anthropogenic
115 emissions (Fig. 1c). The IGP is a large region with varying meteorology and aerosol characteristics,
116 therefore, it is divided into three areas, northwest (NWIGP), central (CIGP), and east (EIGP) which are
117 marked by the black rectangles in Fig.1c. Although biomass burning and anthropogenic emissions
118 dominate throughout the IGP during post-monsoon and winter season, the north-westerly wind system
119 results in the gradient distribution of AOD over this region. The downwind regions, CIGP and EIGP
120 are influenced by the long-range transport from the NWIGP, resulting in high AOD with dominant fine
121 particulates over CIGP and EIGP, especially during post-monsoon and winter (Kedia et al., 2014;
122 Kumar et al., 2018). Therefore, representative stations from each region are considered for the
123 sensitivity analyses. Nine stations have been considered which include, Amritsar, IGI Airport (Indira
124 Gandhi International Airport, Delhi), IHBAS (Delhi), Dwarka (Delhi), RKP (Delhi) in the North-West
125 IGP; Kanpur, Lucknow in Central IGP and Patna, Muzaffarpur in East IGP.

126

2.1 Modeling

128 The WRF-Chem model version 4.0.3 has been used for this study. The model domain is
129 centered at Delhi (77.1°E, 28.7°N) with 300 grid points in the east-west, 170 grid points in the south-
130 north direction (Fig. 1c), and 50 vertical eta levels with the model top at 50 hPa. The horizontal grid
131 spacing of the domain is 10 km, while the vertical grid spacing varies from higher resolution (~200 m)
132 in the boundary layer to coarser resolution (~1200 m) near the model top. To quantify the impact of
133 aerosol-radiation (AR) feedback and aqueous chemistry on the fog properties, we conduct sensitivity
134 simulations (Table 1) for December 20–24, 2017. Three experiments (EXP1, EXP2, and EXP3) have
135 been designed with different combinations of meteorological initial/lateral boundary conditions and
136 planetary boundary layer (PBL) physics to identify the best configuration for meteorological
137 simulations. Experiment 1 (EXP1) uses the National Centers for Environmental Predictions (NCEP)
138 Final Analysis (GFS-FNL; 1° x1°, 6 hourly) meteorology data for initial and boundary conditions and
139 the YSU (Yonsei University; (Hong et al., 2006) PBL scheme. Experiments 2 and 3 (EXP2, EXP3) use
140 ERA-Interim Project (1.125° x 0.703°, 6 hourly) for meteorology initial and boundary conditions, while
141 the PBL options were the YSU PBL scheme and ACM2 (Asymmetric Convective Model version 2)
142 scheme, respectively. ACM2 is a hybrid of the original nonlocal closure (Pleim and Chang, 1992) and
143 a local closure eddy diffusion scheme (Pleim, 2007a, 2007b). The YSU PBL option was coupled with
144 the Noah LSM while ACM2 was coupled with Pleim-Xiu LSM.

145   The advantage of Pleim-Xiu LSM (PX-LSM) is that it allows nudging of soil moisture and

146   temperature to improve the prediction of meteorology near the surface (Xiu and Pleim 2001; Pleim and

147   Xiu 2003; Gilliam et al. 2006) which Noah LSM does not include. The PX-LSM includes two-layer soil

148   (0–1 and 1–100 cm) model, canopy moisture, and aerodynamic and stomatal resistance. Ground surface

149   (1 cm) temperature is calculated from the surface energy balance using a force-restore algorithm for

150   heat exchange within the soil. Although the two-layer approach in PX-LSM is less detailed than the

151   multilayer soil models such as the Noah LSM (four soil layers; Chen and Dudhia 2001), it performs

152   well with realistic initialization for soil moisture and through dynamic adjustment in the model

153   simulation where soil moisture is indirectly nudged according to differences in 2-m temperature (T2)

154   and 2-m relative humidity (RH) between the model and observation (Pleim and Xiu, 2003).Soil moisture

155   nudging adjusts the surface evaporation (direct soil surface evaporation, vegetative evapotranspiration,

156   and evaporation from wet canopies) which then affects the partitioning of available surface energy into

157   latent and sensible heat flux and thus reduces errors in T2 and 2-m RH.

158   For EXP2, meteorological initial conditions were refreshed every 24 hours, while EXP3 was a

159   continuous run but soil moisture was nudged to the Era-Interim dataset to improve the prediction of

160   surface fluxes. All other physics and chemistry options are the same for all the experiments except the

161   surface physics option, which changes with the PBL scheme used. The deposition of cloud droplets is

162   an important moisture and aerosol sink during fog events. For all these simulations, the deposition

163   velocity of cloud droplets was reduced to 0.01 m s^{-1} based on Stoke's Law and previous studies (Katata

164   et al., 2015; Tav et al., 2018) because its default value (0.1 m s^{-1}), is large.

165   To examine the radiative effects of aerosols and aqueous phase chemistry additional simulations

166   have been done using the meteorological configuration in EXP3, with aerosol-radiation (wFB) feedback

167   plus aqueous chemistry (wAq.chem), without aerosol-radiation feedback (nFB) but with aqueous

168   chemistry, and without aqueous chemistry (noAq.chem) but with aerosol-radiation feedback. The

169   analysis has been done for the fog events on 23rd and 24th December 2017 as

170   *Impact of radiation feedback=wFB-nFB*

171   *Impact of aqueous phase chemistry= wAq.chem-noAq.chem*

172   Emissions used in the WRF-Chem simulations are from the EDGAR-*HTAP v2 (Emissions*

173   *Database for Global Atmospheric Research- Hemispheric Transport of Air Pollution;0.1° x 0.1°)*

174   inventory for anthropogenic emissions and *FINN v*2.2 *(Fire INventory from NCAR; 1 km x 1 km)* fire

175   emission inventory (Wiedinmyer et al., 2011). Trash-burning emissions (Chaudhary et al., 2021) are

176   also included in the simulations. The model calculates the biogenic emissions online using MEGAN

177   v2.04 (*Model of Emissions of Gases and Aerosols from Nature*) (Guenther et al., 2006). The initial and

178   lateral boundary conditions for chemical constituents are from the global chemistry transport model

179   CAM-Chem (*Community Atmosphere Model with Chemistry*) (Emmons et al., 2020).

180   The MOZART (Model for Ozone and Related chemical Tracers) chemical mechanism

181   (Emmons et al., 2010) is used for gas-phase chemistry, which includes 85 gas-phase species, 39

182   photolysis, and 157 gas-phase reactions. It has been updated to include an explicit treatment of aromatic

183   compounds HONO, C_2H_2, and isoprene oxidation scheme (Knote et al., 2014). The lumped toluene used

184   by Emmons et al., (2010) has been speciated into benzene, toluene, and lumped isomers of xylenes

185   (Knote et al., 2014). For this study, HCl emissions, transport, dry, and wet deposition are represented.

186   However, HCl gas-phase reaction is not included in MOZART.

187   The Model for Simulating Aerosol Interactions and Chemistry (MOSAIC) with four size bins

188   (0.039–0.156, 0.156–0.625, 0.625–2.500, and 2.5–10.0 µm dry diameters) coupled with MOZART gas-

189   phase chemistry is used (Fast et al., 2006; Zaveri et al., 2008). The bin sizes are defined by their lower

190   and upper dry particle diameters, so there is no transfer of particles between bins during water uptake

191   or loss. It is assumed that aerosols in each bin are internally mixed with the same chemical composition

192   while they are externally mixed in different bins.

193   The aerosol composition includes sulfate (SO_4^{2-}), ammonium (NH_4^-), nitrate (NO_3^-), aerosol

194   water, sea salt (Na^+, Cl^-), methanesulfonate (CH_3SO_3), carbonate (CO_3^{2-}), calcium (Ca^+), black carbon

195   (BC), organic mass (OC), and unspecified inorganic species such as silica, inert minerals, and trace

196   metals lumped together as other inorganic mass (OIN). For OC, primary OC and secondary OC are

197   represented separately, where the latter is simulated using the volatility basis set (VBS) approach.

198   Reactive inorganic species such as potassium (K^+) and magnesium (Mg^+) are usually present in much

199   smaller amounts and are equivalent to Na^+ since their sulfate, nitrate, and chloride salts are similar in

200   terms of their solubility in water.

201   MOSAIC treats condensation and evaporation of trace gases to/from particles, nucleation (new

202   particle formation), and coagulation. Aerosol coagulation (Brownian) is based on (Jacobson et al., 1994)

203   and nucleation is based on (Wexler et al., 1994) parameterization of H_2SO_4-H_2O homogeneous

204   nucleation. Sulfate, nitrate, chloride, and ammonium aerosols are mainly formed through oxidation and

205   neutralization/condensation of gas precursors. Gas-phase sulfuric acid (H_2SO_4) is produced by the gas-

206   phase oxidation of SO_2 by OH and nitric acid (HNO_3) formation is via the oxidation of NO_2 by OH.

207   HCl is a primary emission product. The neutralization/condensation of H_2SO_4, HCl, and HNO_3 with

208   NH_3 produces ammonium such as ammonium sulfate ((NH_4)$_2SO_4$), ammonium bisulfate (NH_4HSO_4),

209   ammonium chloride (NH_4Cl) and ammonium nitrate (NH_4NO_3), respectively. The thermodynamic

210   modules in MOSAIC for the dynamic gas-particle partitioning of aerosols MTEM (Multicomponent

211   Taylor Expansion Method) and MESA (Multicomponent Equilibrium Solver for Aerosols) calculate the

212   activity coefficient in aqueous phase aerosols and compute the intraparticle solid-liquid phase

213   equilibrium respectively (Zaveri et al., 2005, 2008). The Adaptive Step Time-split Euler Method

214   (ASTEM) coupled with MESA-MTEM dynamically integrates the mass transfer equations.

215   Aqueous-phase chemistry uses a bulk water approach employing the Fahey and Pandis (2001)

216   mechanism. It calculates sulfate formation, formaldehyde oxidation, and non-reactive uptake of nitric

217   acid, hydrochloric acid, ammonia, and other trace gases (Chapman et al., 2009; Pye et al., 2020).

218   Aqueous-phase sulfate is produced via oxidation of SO_2 by H_2O_2, O_3, TMI (Transition metal Ion: Fe(III),

219   Mn(II)) catalyzed O_2 and NO_2. TMI concentrations are prescribed in the model to 0.01 µg m^{-3} for Fe(III)

220   and 0.005 µg m^{-3} for Mn(II) (Martin and Good, 1991). The Fe(III) values are within the range of water

221   soluble iron in winter time aerosol reported in India (Kumar and Sarin, 2010). Wet removal

222   (scavenging), is represented by the (Neu and Prather, 2012) scheme for trace gases and Easter et al.,

223   (2004) for aerosols.

224   The WRF-Chem simulations include interactions with radiation, i.e., direct aerosol effect and

225   effect on photolysis rates. Aerosol cloud interactions are not possible when using the ACM2 PBL

226   scheme because the ACM2 PBL scheme does not provide the exchange coefficient for heat, which is

227   required to calculate the activation fraction for mass and number for each bin/mode.

228

229   **2.2 Observations**

230   To evaluate the model output, observations of aerosols and meteorology have been obtained

231   from several satellites as well as ground-based measurement platforms. To examine the aerosol loading

232   and spatial and temporal distribution, daily Level 2 Aerosol Optical Depth (AOD) retrievals from the

233   Moderate Resolution Imaging Spectroradiometer (MODIS) aboard Terra and Aqua satellites are

234   obtained at the spatial resolution of 10 km x 10 km (at nadir) pixel array. It provides aerosol properties

235   from the Dark Target (DT) algorithm applied over the ocean and dark land (e.g., vegetation) and Deep

236   Blue (DB) algorithms over the entire land areas, including both dark and bright surfaces. Each

237   MOD04_L2 (Terra) / MYD04_L2 (Aqua) products are available at a 5-minute time interval with an

238   output grid of 135 pixels in width by 203 pixels in length.

239   The Indian National Satellites (INSAT-3D) in the geostationary orbit at inclinations of 82º

240   longitude provide an imager fog product (3DIMG_L2C_FOG) with a spatial resolution of 4 km every

241   30 min (www.mosdac.gov.in). For daytime, the visible channel observation is used to detect fog,

242   whereas thermal infrared is used to reduce false alarms such as medium/high clouds and snow areas.

243   INSAT 3D's 'day microphysics' data component analyzes solar reflectance at three wavelengths: 0.5

244   µm (visible), 1.6 µm (shortwave infrared), and 10.8 µm (thermal infrared). Night-time fog is derived

245   from TIR-1 (12.0 µm and 10.0 µm) and MIR (10.8 µm and 3.9 µm) channel brightness temperature

246   over the Indian region. INSAT-3D provides fog intensity varying from 1 to 4 indicating SHALLOW

247   for visibility > 600 m; MODERATE, DENSE, and VERY_DENSE, respectively for visibility varying

248   from 0 to 500 m (Banerjee and Padmakumari, 2020). If the visibility is greater than 700 m it indicates

249   no fog while visibility > 1000 m represents very clear skies. Validation of INSAT-3D fog products over

250   the IGP shows a 66%-68% probability of detection and a 10% false alarm rate. It also captures the

251   entire life cycle of fog from formation to dissipation. However, detecting fog during multilayer clouds

252   is still challenging with INSAT-3D (Arun et al., 2018; Chaurasia and Gohil, 2015; Chaurasia and

253   Jenamani, 2017).

254   Ground-based monitoring sites provide hourly data of relative humidity, surface temperature,

255   and wind speed measured by the Central Pollution Control Board, CPCB (http://cpcb.nic.in). In

256   addition, measurements of several aerosols, trace gases, and meteorology at Delhi (IGI Airport) from

257   the Winter Fog Experiment (WiFEX) for the period December 10-31, 2017, have also been used to

258   validate the model output. The WiFEX, an initiative of the Ministry of Earth Sciences (MoES), India,

259   is a ground-based measurement campaign at the IGI Airport Delhi to understand fog's physical and

260   chemical features. Additional details of the WiFEX project and related publications can be found in

261   Ghude et al., (2017).

262

263   **3   Meteorology Evaluation**

264   Previous studies simulating fog highlight the importance of high model vertical resolution

265   (Pithani et al., 2019; Van Der Velde et al., 2010) for representing the fog formation and the growth of

266   the fog layer, model initialization (Yadav et al., 2022), initial relative humidity (Bergot and Guedalia,

267   1994; Pithani et al., 2020), and PBL schemes (Chen et al., 2020; Pithani et al., 2019). In the present

268   study, 2-m relative humidity (RH2), 2-m temperature (T2), and 10-m wind speed (WS) from WRF-

269   Chem have been validated using ground-based measurements from CPCB monitoring network and

270   WIFEX campaign for several stations across the IGP. The NWIGP stations include Amritsar, IGI (Indira

271   Gandhi International Airport), and RKP (Rama Krishna Puram) site in Delhi; Kanpur and Lucknow in

272   central IGP; and Patna in the East IGP. The comparison of WRF-Chem results with observations shows

273   that RH and T2 are sensitive to the choice of the meteorological initial and boundary conditions (Fig.

274   S1). WRF-Chem compares better with the observations for simulations driven by the ERA-Interim

275   reanalysis than with GFS-FNL reanalysis since ERA-Interim provides more realistic RH than GFS-FNL

276   (Figs. S2 a-f). For example, RH from EXP1 (GFS) varies from 10 to 50%, while RH from EXP2 and

277   EXP3 varies from 30 to 100%, which is closer to observation, especially for NWIGP and CIGP. For

278   EIGP, RH from EXP1 (GFS) compares better than ERA-Interim, which overestimates the observed RH.

279   ERA-Interim and YSU PBL scheme showed damping of RH continuously increasing the bias in RH

280   with time (not shown), which was corrected in EXP2 by refreshing meteorology every day at 00h UT

281   during the model simulation. In addition, maps of surface RH and T2 (Figs. S2 g-j) show that the GFS-

282   FNL dataset has lower relative humidity throughout the domain as compared to ERA-Interim. There are

283   differences in simulated 2-m temperature between these two datasets which are of smaller relative

284   magnitude compared to the RH.

285   The GFS-FNL driven meteorology EXP1 has a warm bias in NWIGP and CIGP, especially

286   during night-time, while over EIGP, the model prediction agrees well with observations. EXP2 with the

287   ERA-Interim driven meteorology and YSU PBL scheme also shows good agreement between modeled

288   and observed T2 in EIGP. The ERA-Interim driven meteorology with the ACM2 PBL scheme in EXP3

289   has a cold bias of up to 7°C over EIGP during daytime from 22nd to 24th December. The wind speed

290   evaluation shows that WRF-Chem is over-predicting wind speed. However, it is also possible that some

291   CPCB stations (e.g., Amritsar and RK Puram) have a wind speed low bias due to the low measurement

292   height and obstructions such as tall trees near the monitoring station. Note that at other sites (e.g., over

293   IGI-Delhi and Kanpur) the model measurement agreement is better.

294   The WRF-Chem performance has been statistically assessed against observation using the

295   Taylor Diagram (Taylor, 2001), which provides a statistical summary of how well the model output

296   agrees with the observation in terms of the Pearson correlation, the root-mean-square error (RMSE),

297   and the ratios of their variances (Fig. 2). The percentage bias has also been included to further evaluate

298   the WRF-Chem results. In Fig. 2, better agreement of WRF-Chem results with observations are shown

299   by the marker's proximity to the "OBS" dashed black line. The WRF-Chem RH has a good correlation

300   for all three experiments with $r^2 > 0.75$ at all the locations in IGP for all the experiments. However, the

301   RMSE and the standard deviations are larger for the EXP1. The relative bias is also large ($>20\%$) for

302   EXP1 (GFS-FNL) compared to EXP2 and EXP3 which lie closer to the dashed black line indicating

303   that the simulated RH variations are similar to observations. For all the experiments, WRF-Chem T2

304   agrees well with observations with a correlation between 0.8 and 0.95. The points are concentrated near

305   the dashed line showing a low RMSE and standard deviation for T2, signifying a good agreement of

306   simulated T2 with observation in terms of temporal variation but the T2 relative bias is large for EXP1

307   ($>20\%$). The RMSE and relative bias for EXP1 are larger for several of the stations. The temporal

308   variability of T2 and RH are predicted well for all the combinations of inputs (Fig. S1), however, the

309   accuracy of simulated T2 and RH is sensitive to the choice of meteorological initial/boundary

310   conditions. WRF-Chem predicted RH and T2 agree better with observations when initialized with ERA-

311   Interim meteorology than with GFS-FNL.

312   The WRF-Chem runs driven by ERA-Interim with YSU (EXP2) and ACM2 PBL (EXP3)

313   schemes predicted the surface meteorology better over the IGP than the WRF-Chem run driven by GFS

314   (EXP1). By examining the modeled cloud water content in the lowest model level with the INSAT-3D

315   satellite fog intensity for the 23rd and 24th December 2017 (Fig. 3), it is apparent that WRF-Chem with

316   the ACM2 PBL scheme compared qualitatively well with observations obtained from INSAT-3D

317   satellite in terms of fog coverage over CIGP, while the WRF-Chem run with the YSU PBL scheme did

318   not produce widespread fog. However, there is also fog over EIGP in WRF-Chem with the ACM2 PBL

319   scheme although it is not observed by the satellite. This is because the model has a cold bias in T2 and

320   a high surface RH over East IGP with ACM2 PBL and Pleim-Xiu surface scheme as discussed earlier,

321   which favors the formation of fog in this region. The time series in Fig. 4 shows that EXP3 is capable

322   of predicting the duration of fog on 23rd and 24th December. There is a data gap from INSAT 3D

323   observations because it is unable to capture fog during daytime in the presence of mid and high-level

324   clouds.

325   In conclusion, EXP3 is the best configuration for predicting fog formation where the ERA-

326   Interim meteorology, the ACM2 PBL and surface schemes, and soil moisture nudging is used in the

327   WRF-Chem simulation. Therefore, the evaluation of predicting AOD, surface aerosol concentrations,

328 and aerosol composition as well as analysis of the impact of aerosols on fog formation uses the EXP3

329 configuration.

330

331 **4 Aerosol Evaluation**

332 Aerosol is an important factor in correct prediction of fog (Maalick et al., 2016; Stolaki et al.,

333 2015) as the number of fog droplets depends on the aerosol size distribution and concentration. Aerosols

334 as CCN can affect the liquid water content in fog and therefore an increase in aerosol concentration can

335 significantly affect fog lifetime (Stolaki et al., 2015; Zhang et al., 2014b). AOD retrievals from the

336 MODIS satellite have been used to validate the modeled AOD (Fig. 5). It is observed that the model

337 captures several important features of the MODIS retrieved AOD spatial distribution but at the same

338 time somewhat struggles to reproduce the observed AOD magnitude in some parts of the domain. One

339 possible reason for the underestimation would be the EDGAR-HTAP emission inventory, which has a

340 low bias for residential sector $PM_{2.5}$ emissions in India (Sharma et al., 2022). For instance, the model

341 successfully predicts high aerosol loading seen by MODIS on 20 and 21 December over CIGP and

342 EIGP. This is the region with dense fog both in model and observation. Higher AOD (>0.5) over CIGP

343 and EIGP can be attributed to the accumulation of aerosols that are transported by north-westerly winds

344 to these regions from NWIGP (Dey and Di Girolamo, 2011; Jain et al., 2020; Jethva et al., 2018; Kumar

345 et al., 2018; Yadav et al., 2020). However, WRF-Chem underestimates AOD over the NWIGP

346 (AOD<0.3) throughout the simulation period and during 23-24 December over CIGP and EIGP where

347 the latter may be related to enhanced scavenging of aerosols by fog droplets.

348 The west to east gradient in aerosol loading over IGP is consistent with surface $PM_{2.5}$

349 distribution (Fig. 6a). Surface $PM_{2.5}$ concentration is highest in EIGP (>100 µg/m^3) and it decreases

350 gradually towards NWIGP (~60-80 µg/m^3). The time series of $PM_{2.5}$ from CPCB measurements and the

351 model at stations representative of each region in IGP shows that simulated $PM_{2.5}$ compares well with

352 observation in terms of day-to-day variation over most of the locations in the IGP (Fig. 6 b-e). The

353 comparison is good over Amritsar (an NWIGP location), where $PM_{2.5}$ is mostly primary aerosols from

354 local emissions e.g., residential heating related biomass burning. Agricultural waste burning is at its

355 peak during post monsoon months (Oct-Nov) whereas during winter burning for residential heating

356 increases and the stable boundary layer confines these emissions near the surface (Kumar et al., 2021;

357 Pawar and Sinha, 2022). $PM_{2.5}$ at Amritsar shows a bimodal distribution with morning and evening

358 peaks whereas it is absent in the model likely due to the absence of diurnal variations in the WRF-Chem

359 anthropogenic emissions.

360 At Delhi, the daily variations are predicted well although WRF-Chem underestimates $PM_{2.5}$

361 observations during the first 4 days. Delhi experiences severe air pollution and haze with high PM

362 loading (> 500 µg m^{-3}) (Bharali et al., 2019). The model is successful in predicting the high $PM_{2.5}$

363 episode on the 24th of Dec. However, it fails to predict the composition correctly (Fig. 7). Although

364 simulated SO_2 and NH_3 are comparable with observation, sulfate, and ammonium are underestimated

365   in the model. SO_4^{2-} is underestimated by ~ 9 µg m^{-3}, while NH_4^+, NO_3^- and Cl^- are underestimated by

366   ~30 µg m^{-3}, ~19 µg/m^3 and ~40 µg/m^3 on average, respectively. This leads to the underestimation of

367    $PM_{2.5}$ over Delhi. Studies report very high chloride over the IGP with values exceeding 100 µg m^{-3}

368   (Lalchandani et al., 2021) during winter emitted from increased trash burning and industrial emissions

369   (Pant et al., 2015; Patil et al., 2013). Our model includes HCl emissions from trash burning but emissions

370   from other sources (e.g., industries) are unaccounted for in the model which likely leads to the

371   underestimation in modeled chloride.

372   Over the CIGP and EIGP, the underestimation in $PM_{2.5}$ is mostly observed at the east IGP

373   locations during the dense fog. It is well known that the hygroscopic aerosols grow in size and are

374   deposited to the surface during fog (Gupta and Mandariya, 2013; Kaul et al., 2011). $PM_{2.5}$ shows an

375   increase initially with the onset of fog and then it decreases as the aerosols grow and get deposited

376   through fog droplets. A two order higher deposition rate (Fig. 6 f, g) during fog compared to the

377   deposition rate of dry aerosol results in the lower $PM_{2.5}$ over CIGP and EICP during fog events.

378   Previous studies have reported that models tend to underestimate the AOD observation (David

379   et al., 2018; Pan et al., 2015) during the post-monsoon and winter when agricultural waste burning and

380   anthropogenic emissions dominate. While anthropogenic emissions include a contribution from the

381   residential sector, the emissions from small-scale burning for residential heating over IGP especially

382   during winter are likely underestimated in the current emission inventory (Sharma et al., 2022). This

383   leads to an underestimation of aerosol concentration in the model. Other possible causes for the

384   underestimation are the biases in the simulated meteorology (Govardhan et al., 2015; Kumar et al., 2015;

385   Pan et al., 2015) which affects the aerosol concentration. We corrected some of the biases in

386   meteorology as discussed earlier however there are still residual biases in the simulated meteorology

387   e.g., overestimation of wind speed by WRF-Chem. We also observe underestimation of secondary

388   aerosols over NWIGP which contribute significantly to the aerosol loading over IGP. Secondary aerosol

389   formation is substantial over CIGP and EIGP in the model compared to NWIGP which will be discussed

390   in a later section. Several modeling studies have shown significant improvements in forecasting surface

391    $PM_{2.5}$ by assimilation of satellite AOD and $PM_{2.5}$ (Ghude et al., 2020; Jena et al., 2020; Kumar et al.,

392   2020) suggesting the importance of correct initialization of the model in simulating aerosols over IGP.

393

394   **5   Effect of Aerosol Radiation feedback**

395   Interactions of aerosols with radiation affects temperature and surface heat fluxes, thereby

396   weakening the turbulence in the PBL and stabilizing the boundary layer height (Fig. 8b) compared to

397   the clean environment (Fig. 8a). In the presence of well mixed aerosols within the PBL, the radiative

398   effect of aerosols lowers the noontime PBL height (Fig. 8b). However, the presence of absorbing

399   aerosols in the PBL warms the air and changes the thermodynamics. Three cases are shown in Fig. 8(c-

400   e) where increases of scattering aerosol concentrations at the top of PBL (Fig. 8c) increases scattering

401   of radiation by the aerosol layer and reduces the surface reaching solar radiation similar to Fig. 8b.

402 Higher concentrations of absorbing aerosols at the top of PBL (Fig. 8d) warms the air above the
403 boundary layer and strengthens the capping inversion stabilizing the PBL and suppressing its growth.
404 The shallow PBL and weakened daytime vertical mixing confines aerosols and water vapor near the
405 surface and worsens the air quality of a region. The aerosols trapped in the stagnant PBL further affects
406 the radiation flux at the surface and creates a positive feedback loop wherein the PBL is continually
407 suppressed until interrupted by some synoptic weather phenomenon, such as the western disturbances
408 in the IGP. On the other hand, higher concentration of absorbing aerosols within the PBL (Fig. 8e)
409 warms the air in the PBL and this results in the higher PBL height. The raised PBL decreases the aerosol
410 concentration near the surface which is termed as a negative feedback effect.

411 The aerosol radiation feedback can affect shortwave heating rates (SWHR). The high aerosol
412 loading over the IGP (Fig. 6 and Fig. 7) allows the AR feedback to reduce the PBL height by more than
413 140 m throughout the IGP compared to the surrounding region with AR feedback (Fig. 9a). The
414 difference in PBL height with and without aerosol radiation feedback is largest during noontime. The
415 suppressed PBL is due to the decrease in the surface heating flux and the consequent weakening of
416 turbulence in the PBL. The surface solar radiation flux (SWF) decreases by 5-35 % while the surface
417 latent heat (LH) and sensible heat (HFX) fluxes decrease by 5-35 % and 10-60 %, respectively (Fig.
418 S3). The stable, shallow PBL reduces the vertical mixing of aerosols and moisture and confines them
419 near the surface, resulting in increased $PM_{2.5}$ concentrations and RH near the surface with AR feedback
420 (Fig. 9). Although T2 should decrease with the reduction in surface SWF, T2 shows mixed signals with
421 both cooling and warming over IGP. While surface cooling is observed over NWIGP and EIGP, T2
422 increases with AR feedback over most of CIGP. The response of AR feedback to T2 varies in these
423 three regions probably due to differences in the distribution and types of aerosols and the presence of
424 fog. Increase in surface concentration of $PM_{2.5}$ occurs more over NWIGP and EIGP with increase in BC
425 and OIN over NWIGP, and sulfate aerosol over EIGP which results in the surface cooling due to positive
426 AR feedback in these two regions.

427 Over the CIGP, the AR feedback causes a depletion of surface $PM_{2.5}$ (Fig. 9d). Examining
428 further, the time variation of the changes in PBL height, T2, and RH between the simulations with and
429 without aerosol-radiation feedback (Fig. 9g) shows an increase in T2 while the surface fluxes, sensible
430 heat flux, latent heat flux, and downward shortwave radiation flux decrease over CIGP (Fig. 9h). AR
431 feedback affects mostly the lower atmosphere at multiple levels; however, our finding suggests that the
432 decreased shortwave radiation flux decreases the surface fluxes and thus the turbulence in the boundary
433 layer resulting in a reduced PBL height on both days. Figure 9 g and h clearly show a decrease in HFX
434 and LH following the decrease in SWF. Moreover, we observe that the PBL height is sensitive to latent
435 heat flux likely due to its strong dependence on moisture availability (Xiu and Pleim, 2001; Zhang and
436 Anthes, 1982).

437 The impact of AR feedback on T2 depends on factors such as the presence of absorbing aerosols
438 and their vertical distribution via heating or increased SWF (as observed in CIGP, Fig. S3). Absorbing

439   aerosols in WRF-Chem include BC and OIN (other inorganic aerosols), which both increase near the

440   surface (Fig. 9e, Fig. S4) due to their confinement in the stable PBL. Some areas in the fog-affected

441   region show a decrease in BC as well as SO_4^{2-} which is likely due to their hygroscopic growth, increase

442   in activation to fog droplets, and then dry deposition in dense fog. The increase in RH favours the growth

443   of aerosols in size by the uptake of water and also the formation of secondary aerosols. As a result, AR

444   feedback changes the absorbing to scattering ratio of aerosols over IGP indicated by the decrease in

445   SSA (Single Scattering Albedo; Fig. S5). A decrease in SSA is found in CIGP throughout the boundary

446   layer while it is negligible in NWIGP. SSA increases in EIGP in the PBL and decreases near the top of

447   PBL. Similar observation has been made by Ramachandran et al., (2020) where SSA decreases with

448   increasing altitude due to absorbing carbonaceous aerosols at higher elevations which contributes ≥75%

449   to the aerosol absorption over IGP. Increased shortwave heating (Fig. 10) is probably caused by the

450   increased absorbing aerosols near the surface which overwhelms the surface cooling due to reduced

451   shortwave radiation at the surface.

452   The increase in 2-m RH is substantial over CIGP on 24th December (Fig. 9g) compared to the

453   previous day following the decrease in PBL height which constrains the moisture near the surface. The

454   decrease in RH by 2% or more when aerosol-radiation feedback is included compared to no aerosol-

455   radiation feedback is likely due to increase in T2. However, the increase in RH in the afternoon

456   associated with a decrease in LH and PBL height is important for the air to saturate which then favors

457   the formation of fog in a polluted environment. Note that the increase in T2 with AR feedback is very

458   small (<0.5°C) which reduces further after noon (~12:30 pm IST) on both days.

459   Another important factor that can affect the extent of change in PBL height is the distribution

460   of aerosols in the vertical (illustrated in Fig. 8). The pressure-time cross-sections of differences in T,

461   $PM_{2.5}$, BC, and SO_4^{2-} between aerosol radiation (AR) feedback (wFB) and no aerosol radiation feedback

462   (nFB) for three regions, NWIGP, CIGP, and EIGP are shown in Fig. 11. The difference in the PBL

463   height reaches a maximum with the AR feedback during midday (12:30-15:30 IST). Increase in

464   temperature in the boundary layer is observed with AR feedback particularly at the upper PBL in all the

465   regions of IGP. This induces a temperature inversion resulting in a stable and suppressed PBL. In all

466   the regions the decrease in PBL height (100-200 m) is larger on 24th December compared to 23rd

467   December. The difference in the PBL height on 23rd and 24th December with AR feedback on these days

468   is possibly controlled by the aerosol distribution during the previous day or early morning on the same

469   day. For example, in all the regions an increase in $PM_{2.5}$ is observed the previous night (23:30 onwards)

470   till ~11:30 of December 24, with increased BC over NWIGP and CIGP whereas both BC and SO_4^{2-} over

471   EIGP. The increased $PM_{2.5}$ concentrations suppress the development of the PBL after sunrise with AR

472   feedback on December 24 compared to that on December 23, leading to the observed differences in

473   ΔPBL height on these two days. Increase in BC concentrations in NWIGP and CIGP are found above

474   the PBL on 24th December whereas BC concentrations decrease within the PBL. This BC concentration

475   gradient creates a temperature inversion, for example between 10:30-14:30 IST. The increase in BC

476   warms the air in the PBL; however, the warming is not strong enough to cause negative feedback over

477   CIGP. On 23rd December a small increase in BC is uniform throughout the PBL, while there is a decrease

478   in SO_4^{2-} concentrations, resulting in a warmer PBL (Fig. 11) with AR feedback.

479   In EIGP, BC distribution is similar to that in CIGP with AR feedback while there is a substantial

480   increase in sulfate aerosol in the PBL. This results in the strongest extinction in EIGP as evident from

481   the largest difference in PBL height and surface cooling with AR feedback among the three regions.

482   Although ΔPBL is small on 23rd December, it still results in the accumulation of aerosols during night-

483   time (~23:30 pm onwards) which further strengthens the AR feedback effect the next day in NWIGP

484   and CIGP. Thus, AR feedback stabilizes the PBL, increases $PM_{2.5}$ and RH in the PBL making conditions

485   favourable for persistence of fog over IGP.

486

487   **6   Effect of Aqueous phase chemistry**

488   In this section we discuss the impact of aqueous phase chemistry on aerosol composition and

489   its interaction with meteorology. There is a considerable difference in the surface concentration of $PM_{2.5}$

490   (>16 µg m^{-3}) in the absence of aqueous chemistry over CIGP and EIGP where fog occurs (Fig. 12a)

491   while the difference is negligible over NWIGP where fog does not occur. This is due to the formation

492   of secondary aerosols through aqueous phase chemistry and the hygroscopic growth of aerosols during

493   fog in these regions with the inclusion of aqueous chemistry in the model. In the region between CIGP

494   and EIGP (83E-84E; marked by the box in Fig. 12a), $PM_{2.5}$ concentration is less in the simulation with

495   aqueous-phase chemistry than without aqueous-phase chemistry because deposition of fog water

496   aerosols to the surface increases as the fog thickens (Fig. 13, Fig. S6). Figure 13 shows the relation

497   between formation of secondary aerosols, deposition flux of $PM_{2.5}$, and fog with and without aqueous

498   phase chemistry. During the fog event, the secondary aerosols (SO_4^{2-}, NH_4^+) increase significantly by

499   4-10 µg m^{-3} due to aqueous phase chemistry adding to the $PM_{2.5}$ burden over IGP. The intensity of fog

500   is high around midnight December 24-25 compared to that on 23rd and 24th (1:30-11:30 IST)) which

501   increases the dry deposition flux of $PM_{2.5}$ causing a sharp drop in the $PM_{2.5}$ concentration on 24th

502   December compared to the previous night's fog event. The observed change in $PM_{2.5}$ over a region is

503   the net result of the formation of secondary aerosols and its deposition with fog droplets.

504   The composition distribution of $PM_{2.5}$ (Fig. 12b) has a similar distribution for the simulations

505   with and without aqueous phase chemistry over NWIGP where fog did not occur. The primary aerosols

506   are higher (BC > 9%, OC ~ 16-30%, OIN > 50%), than the secondary aerosols (<5%). While the model

507   requires fog for accelerated formation of secondary inorganic aerosol, experimental data (Fig. 7)

508   supports significant formation of secondary inorganic aerosol at elevated RH levels even in haze aerosol

509   (Acharja et al., 2022). On the other hand, the central and east IGP stations are fog-covered and therefore,

510   there is an increase in secondary aerosols esp. SO_4^{2-} and NH_4^+ when aqueous phase chemistry is included

511   in the simulation. SO_4^{2-} is chemically produced via aqueous phase chemistry in cloud water, hence the

512   abrupt increase whereas NH_4^+ maintains a gas-aerosol and gas-cloud equilibrium with NH_3 and SO_4^{2-}

513   via neutralizing the drop or aerosol. NO_3^- is high in the model compared to SO_4^{2-} and NH_4^+ and it

514   decreases by ~1-2 % with aqueous phase chemistry. We observe a small increase in NO_3^- during fog,

515   however it drops as fog intensifies, more rapidly than that without aqueous phase chemistry likely due

516   to increase in dry deposition. This results in lower average NO_3^- to $PM_{2.5}$ ratio with aqueous phase

517   chemistry. Moreover, NO_3^- is high over the fog covered CIGP and EIGP compared to NWIGP

518   suggesting that transport and chemistry of NO_x in CIGP and EIGP produce more HNO_3. Aerosol NO_3^-

519   is also in equilibrium with HNO_3 and it is formed only if excess NH_3 is available beyond the sulfate

520   neutralization. Thus, NH_4^+ and NO_3^- changes are likely due to changing the partitioning between gas

521   and liquid based on the production of sulfate.

522         $PM_{2.5}$ is mostly composed of organic aerosols (OA) over CIGP and EIGP whereas it is OIN

523   (dust) and OA over NWIGP. Although observational studies report Cl^- as one of the largest contributors

524   (12-17%) to $PM_{2.5}$ after the organics (Lalchandani et al., 2021; Pant et al., 2015) during winter, Cl^- is

525   largely underestimated by the model as discussed in section 4 and contributes only ~3%. A small

526   increase (2-4%) in secondary organic aerosols (SOA) from glyoxal production in aerosols occurs for

527   the simulation with aqueous phase chemistry included during intense fog, suggesting there are feedbacks

528   between cloud chemistry (without glyoxal aqueous chemistry) and aerosol chemistry. However, similar

529   to NO_3^-, average SOA (ASOA (anthropogenic)+BSOA (biogenic) + GlySOA) shows a decrease when

530   aqueous phase chemistry is included. SOA contributes significantly to organic aerosol loading over IGP

531   (Kaul et al., 2011; Mandariya et al., 2019).

532   The WRF-Chem results on aerosol composition behave similarly to observational studies. For

533   example, Ram et al., (2012) reported an increase of EC, OC, and WSOC concentrations by ~30% during

534   fog and haze events at Allahabad, a location in the Central IGP, and a marginal increase of these

535   constituents at Hisar (NWIGP). Several studies report an increase in inorganic ions (NH_4^+, NO_3^-, and

536   SO_4^{2-}) during fog over IGP and elsewhere (Gundel et al., 1994; Ram et al., 2012). Recent studies suggest

537   that a significant fraction of atmospheric particulate matter in the IGP is comprised of carbonaceous

538   aerosol (~30–35% of the PM) and water-soluble inorganic species (~10–20% of the PM) during

539   October−January when emissions from biomass burning (including residential heating) are dominant

540   over IGP (Ram et al., 2014; Rengarajan et al., 2007; Tare et al., 2006).

541   Both the simulations with and without aqueous-phase chemistry include the AR feedback. The

542   increased $PM_{2.5}$ with aqueous phase chemistry interacts with radiation and adds to the AR feedback.

543   Since the secondary inorganic aerosols are scattering aerosols, the increased scattering of radiation

544   further reduces the solar radiation reaching the surface (Fig. 14a). Over CIGP the presence of higher

545   aerosol loading reduces the T2 during daytime, particularly on the 24th of December which then reduces

546   the PBL height and increases RH near the surface (Fig. 14b). These conditions favor fog formation over

547   the CIGP. Further, the fog water content with aqueous-phase chemistry is higher than that without

548   aqueous-phase chemistry on 24th December post-midnight (Fig. 13b). This is likely due to saturation of

549   air due to increase in RH and lower T2, induced by the AR feedback caused by the increase in PM$_{2.5}$.

550   Although the difference in T2 is small (<0.4), favourable conditions mentioned above are conducive to

551   fog formation. Another reason for increase in fog water content is the increase in the size of aerosols

552   such as sulfate which grows in size by water uptake and are activated to form fog.

553

554   **7   Effect of AR feedback and aqueous chemistry on the duration of fog**

555   Aerosol and its radiative effects impact the lifetime of fog over a region and hence its

556   distribution. Figure 15(a) shows the time-series of fog liquid water content (LWC) from WRF-Chem

557   and fog intensity from INSAT-3D satellite similar to Fig. 4, for all three experiments with aqueous

558   chemistry plus AR feedback, aqueous chemistry without AR feedback, and without aqueous chemistry

559   but with AR feedback). The fog starts forming one hour earlier with AR feedback than without AR

560   feedback. In the simulation without aqueous phase chemistry, fog formation is delayed by an hour or

561   two compared to the simulation with aqueous chemistry plus AR feedback. Fog cover occurs for both

562   the simulations with and without aqueous chemistry, however the fog water content is greater with

563   aqueous chemistry than without aqueous chemistry. Fog dissipation usually occurs after sunrise when

564   the shortwave radiative warming at the surface warms the air, which results in PBL mixing. In addition,

565   absorbing aerosols like BC affect fog dissipation by increasing the radiative heating in and above the

566   fog. We find an increase in BC and shortwave heating in the PBL with AR feedback (Fig. 10,11) and

567   warming over CIGP with AR feedback. Fog intensity starts to decrease after 01 UTC (06:30 IST),

568   however, in our study, we find that the fog dissipates completely in the afternoon (~10 UTC or 15:30

569   IST) for both the simulations with AR feedback and no aqueous chemistry while an hour later without

570   AR feedback. The AR feedback induces radiative cooling of the surface and increases surface PM$_{2.5}$,

571   which contributes to fog as CCN. Increase in CCN at 0.02% supersaturation, a value typical of fog, is

572   observed on 24th December with AR feedback as compared to no AR feedback (Fig. 15b). As discussed

573   in earlier sections the impact of AR feedback is more on 24th December than that on 23rd which increases

574   RH and CCN on 24th. This facilitates the growth of aerosol and their activation to form fog droplets.

575   Thus, AR feedback produces more fog droplets in polluted conditions and makes fog dense as indicated

576   by the rapid increase in LWC with AR feedback. Shao et al. (2023) examined aerosol-fog interactions

577   for two consecutive fog events by comparing WRF-Chem results with current emissions strengths to

578   those with low emission strengths. They show that the first fog event promotes formation of the second

579   fog event leading to wider fog distribution, and longer fog lifetime favoured by multiple feedbacks

580   including AR feedback i.e., low temperature, high humidity and high stability similar to our study.

581   While Shao et al. (2023) observe a delay in dissipation of the first event and early formation of second

582   fog event, we find an early dissipation and early formation of fog with AR feedback as discussed earlier

583   in this section. Dry deposition (ddmass) also increases in dense fog which causes rapid loss in CCN and

584   activated aerosols during fog with AR feedback as in Fig. 15 (b and c). Thus, aqueous phase chemistry

585   together with AR feedback promotes early formation of fog while AR feedback alone promotes early

586   dissipation of fog and plays a critical role in the formation and evolution of the fog over IGP.

587

588   **8 Conclusions**

589   The effects of aerosol-radiation (AR) feedback and aqueous chemistry in air quality and fog

590   have been assessed over IGP. We carried out three experiments using WRF-Chem testing different

591   combinations of PBL schemes and meteorology initial and boundary conditions. The best representation

592   of surface meteorology for the IGP region for the case study (December 20-25, 2017) used ERA-Interim

593   reanalysis to drive the meteorology and ACM2 PBL scheme with soil moisture nudging to ERA-Interim.

594   With this meteorology configuration for WRF-Chem, evaluation of aerosol concentrations with

595   measurements and the impact of aerosols on atmospheric processes during fog were examined. AOD

596   regional distribution is predicted well by the model for most of the IGP. However, AOD is

597   underestimated over NWIGP likely due to an underestimation of fugitive emissions during wintertime

598   cold spells. $PM_{2.5}$ daily variation concentrations are predicted well over IGP however secondary

599   aerosols are underestimated. Increased dry deposition of $PM_{2.5}$ with cloud water droplets is observed

600   during fog.

601   The AR interactions showed a significant impact on meteorology and air quality over IGP. A

602   WRF-chem simulation with AR interactions resulted in a lower PBL height by ~50-270 m compared to

603   a simulation without AR interactions leading to accumulation of aerosols and moisture near the surface.

604   Reduced surface shortwave radiation flux and the surface sensible and latent heat fluxes due to aerosol

605   radiative effect suppressed the turbulence resulting in a stable PBL. The shallow PBL further increased

606   surface $PM_{2.5}$ (> 8 ug m^{-3}) and RH (2-8%) over IGP and this positive feedback mechanism promoted

607   thickening of fog over IGP. However, an increase in absorbing aerosols in the PBL gave negative

608   feedback, increasing the shortwave heating and temperature particularly over CIGP. Fog forms when

609   air is saturated which occurs when the surface temperature is reduced or the moisture content increases

610   causing saturation of air. This study suggests that increase in RH saturated the air and the increase in

611   aerosols favoured fog formation as depicted by the thickening of fog intensity. Aqueous phase chemistry

612   on the other hand contributed significantly to secondary aerosols in the fog, especially sulfate aerosols,

613   indicating substantial formation of secondary aerosols in the cloud. The underpredicted secondary

614   aerosols over NWIGP where no fog occurred implies underestimation of formation of aerosols through

615   gas and aerosol chemistry in the model. This underestimation could also be linked to an underestimation

616   of pH in the default MOSAIC scheme (Ruan et al., 2022) which slows the secondary aerosol formation,

617   or an underestimation of the aqueous sulfur oxidation in haze aerosol at > 80% RH before the onset of

618   fog (Acharja et al., 2022), or missing multiphase oxidation processes (Wang et al., 2022). We also

619   observed that AR feedback with aqueous chemistry initiated the fog formation 1-2 hours earlier than

620   the initiation time in the simulation without AR feedback and without aqueous phase chemistry whereas

621   AR feedback alone led to early dissipation of fog. In addition, fog acted as an important sink of aerosols

622   in a polluted environment with increased dry deposition with cloud water. Thus, AR feedback and

623   aqueous chemistry play a significant role in modulating the distribution and concentration of aerosols

624   and evolution of fog in the PBL.

625   The large emission of aerosols and trace gases in the IGP makes the atmospheric dynamics as

626   well as chemistry complex, suggesting the need for more studies using both models and ground-based

627   measurements to better understand the processes. While all aerosol types interact with solar radiation

628   and reduce the surface reaching flux, presence of absorbing aerosols in the boundary layer and its

629   vertical distribution plays an important role in modulating the meteorology over IGP. It is therefore

630   crucial to improve the simulation of absorbing aerosols e.g., BC in the vertical as well as at the surface

631   to increase the accuracy in predicting formation as well as the dissipation of fog in this region. Emissions

632   from burning for residential heating are an important source of aerosols in IGP during post-monsoon

633   and winter and the inclusion of these sources in the emission inventory would improve the prediction

634   of wintertime aerosols. For example, the underestimation of chloride aerosol in the model indicates

635   unaccounted emission sources over IGP. Additionally, more detailed modeling studies are required to

636   understand the missing chemical processes if any in the model which leads to biases in sulfate-nitrate

637   and ammonium partitioning between gas and aerosol phases. We find that the change in PBL height

638   with AR feedback is sensitive to changes in LH, signifying the role of soil moisture in PBL dynamics.

639   Several studies have reported cooling over IGP due to an increase in irrigation (Kumar et al., 2017;

640   Mishra et al., 2020). Further investigations into the role of irrigation in the increasing fog events over

641   NWIGP would help in better understanding the formation and persistence of fog over this region. It can

642   be concluded that fog forecasting is a complex process due to the multiple factors involved and this

643   work suggests that AR feedback is important in fog forecasting while aqueous phase chemistry plays

644   an important role in defining the composition of aerosols over IGP.

645

646   **Acknowledgement**

647   This work is funded by the National Center for Atmospheric Research (NCAR), sponsored by the

648   National Science Foundation. CB is thankful to the Fulbright Kalam Climate Fellowship program under

649   USIEF (United States – India Educational Foundation), and Women Scientist (WOS-A) program,

650   Department of Science and Technology (DST), Govt of India. The authors acknowledge the use of

651   MODIS data from NASA's Land, Atmosphere Near real-time Capability for EOS (LANCE) system

652   (https://earthdata.nasa.gov/lance), part of NASA's Earth Observing System Data and Information

653   System (EOSDIS); Meteorological & Oceanographic Satellite Data Archival Centre (MOSDAC:

654   https://www.mosdac.gov.in/), Space Applications Centre, Indian Space Research Organisation, Govt.

655   of India for INSAT-3D fog data and the Central Pollution Board of India (CPCB:

656   https://app.cpcbccr.com/ccr/#/login) for meteorology data. We would like to acknowledge the high-

657   performance computing support from Cheyenne (doi:10.5065/D6RX99HX) provided by NCAR's

658   Computational and Information Systems Laboratory. We thank Duseong Jo and Behrooz R for their
659   constructive comments on the manuscript.
660
661   **Data availability:** All the model simulations are archived on the NCAR campaign storage
662   (/glade/campaign/acom/acom-weather/chandrakala) and can be accessed by contacting the
663   corresponding author. WIFEX data can be made available by contacting Dr S.D. Ghude. Trash Burning
664   emission data is available on Mendeley data (doi- http://dx.doi.org/10.17632/t2tn4t9473.1). MODIS
665   AOD retrievals can be downloaded from https://earthdata.nasa. gov/.
666
667   **Author contributions:**
668   CB: Conceptualization, Formal Analysis, Writing
669   MB: Conceptualization, Supervision, Writing-review and editing, Funding acquisition
670   RK: Conceptualization, Supervision, Writing-review and editing
671   SDG: provided ground-based observation data, Writing-review and editing
672   VS and BS: provided trash burning emission data, Writing-review and editing
673
674   **Competing interests:** The authors declare that they have no conflict of interest.
675

676   **References**

677   Acharja, P., Ali, K., Ghude, S. D., Sinha, V., Sinha, B., Kulkarni, R., Gultepe, I. and Rajeevan, M. N.:
678   Enhanced secondary aerosol formation driven by excess ammonia during fog episodes in Delhi, India,
679   Chemosphere, 289(July 2021), 133155, doi:10.1016/j.chemosphere.2021.133155, 2022.

680   Arun, S. H., Sharma, S. K., Chaurasia, S., Vaishnav, R. and Kumar, R.: Fog/low clouds detection over
681   the delhi earth station using the ceilometer and the insat-3d/3dr satellite data, Int. J. Remote Sens.,
682   39(12), 4130–4144, doi:10.1080/01431161.2018.1454624, 2018.

683   Badarinath, K. V. S., Kumar Kharol, S. and Rani Sharma, A.: Long-range transport of aerosols from
684   agriculture crop residue burning in Indo-Gangetic Plains—A study using LIDAR, ground measurements
685   and satellite data, J. Atmos. Solar-Terrestrial Phys., 71(1), 112–120,
686   doi:https://doi.org/10.1016/j.jastp.2008.09.035, 2009.

687   Banerjee, S. and Padmakumari, B.: Spatiotemporal variability and evolution of day and night winter fog
688   over the Indo Gangetic Basin using INSAT-3D and comparison with surface visibility and aerosol
689   optical depth, Sci. Total Environ., 745, 140962, doi:10.1016/j.scitotenv.2020.140962, 2020.

690   Bergot, T. and Guedalia, D.: Numerical Forecasting of Radiation Fog. Part I: Numerical Model and
691   Sensitivity Tests, Mon. Weather Rev., 122(6), 1218–1230, doi:10.1175/1520-
692   0493(1994)122<1218:NFORFP>2.0.CO;2, 1994.

693   Bharali, C., Nair, V. S., Chutia, L. and Babu, S. S.: Modeling of the Effects of Wintertime Aerosols on
694   Boundary Layer Properties Over the Indo Gangetic Plain, J. Geophys. Res. Atmos., 124(7), 4141–4157,
695   doi:10.1029/2018JD029758, 2019.

696   Bodaballa, J. K., Geresdi, I., Ghude, S. D. and Salma, I.: Numerical simulation of the microphysics and
697   liquid chemical processes occur in fog using size resolving bin scheme, Atmos. Res., 266, 105972,
698   doi:https://doi.org/10.1016/j.atmosres.2021.105972, 2022.

699   Boutle, I., Price, J., Kudzotsa, I., Kokkola, H. and Romakkaniemi, S.: Aerosol-fog interaction and the
700   transition to well-mixed radiation fog, Atmos. Chem. Phys., 18(11), 7827–7840, doi:10.5194/acp-18-
701   7827-2018, 2018.

702   Chapman, E. G., Gustafson, W. I., Easter, R. C., Barnard, J. C., Ghan, S. J., Pekour, M. S. and Fast, J.
703   D.: Coupling aerosol-cloud-radiative processes in the WRF-Chem model: Investigating the radiative
704   impact of elevated point sources, Atmos. Chem. Phys., 9(3), 945–964, doi:10.5194/acp-9-945-2009,
705   2009.

706   Chaudhary, P., Garg, S., George, T., Shabin, M., Saha, S., Subodh, S. and Sinha, B.: Underreporting
707   and open burning – the two largest challenges for sustainable waste management in India, Resour.
708   Conserv. Recycl., 175(July), 105865, doi:10.1016/j.resconrec.2021.105865, 2021.

709   Chaurasia, S. and Gohil, B. S.: Detection of Day Time Fog over India Using INSAT-3D Data, IEEE J.
710   Sel. Top. Appl. Earth Obs. Remote Sens., 8(9), 4524–4530, doi:10.1109/JSTARS.2015.2493000, 2015.

711   Chaurasia, S. and Jenamani, R. K.: Detection of Fog Using Temporally Consistent, , 10(12), 5307–
712   5313, 2017.

713   Chen, C., Zhang, M., Perrie, W., Chang, R., Chen, X., Duplessis, P. and Wheeler, M.: Boundary Layer
714   Parameterizations to Simulate Fog Over Atlantic Canada Waters, Earth Sp. Sci., 7(3),
715   doi:10.1029/2019EA000703, 2020.

716   David, L. M., Ravishankara, A. R., Kodros, J. K., Venkataraman, C., Sadavarte, P., Pierce, J. R.,
717   Chaliyakunnel, S. and Millet, D. B.: Aerosol Optical Depth Over India, J. Geophys. Res. Atmos.,
718   123(7), 3688–3703, doi:10.1002/2017JD027719, 2018.

719   Debnath, S., Karumuri, R. K., Govardhan, G., Jat, R., Saini, H., Vispute, A., Kulkarni, S. H., Jena, C.,
720   Kumar, R., Chate, D. M. and Ghude, S. D.: Implications of Implementing Promulgated and Prospective
721   Emission Regulations on Air Quality and Health in India during 2030 N3 - 10.4209/aaqr.220112,
722   AEROSOL AIR Qual. Res. [online] Available from: http://hdl.handle.net/10754/681704, 2022.

723   Dey, S. and Di Girolamo, L.: A decade of change in aerosol properties over the Indian subcontinent,
724   Geophys. Res. Lett., 38(14), 1–5, doi:10.1029/2011GL048153, 2011.

725   Dey, S. and Tripathi, S. N.: Estimation of aerosol optical properties and radiative effects in the Ganga

726   basin,   northern   India,   during   the   wintertime,   J.   Geophys.   Res.   Atmos.,   112(3),

727   doi:10.1029/2006JD007267, 2007.

728   Dhangar, N. G., Lal, D. M., Ghude, S. D., Kulkarni, R., Parde, A. N., Pithani, P., Niranjan, K., Prasad,

729   D. S. V. V. D., Jena, C., Sajjan, V. S., Prabhakaran, T., Karipot, A. K., Jenamani, R. K., Singh, S. and

730   Rajeevan, M.: On the Conditions for Onset and Development of Fog Over New Delhi: An Observational

731   Study from the WiFEX, Pure Appl. Geophys., 178(9), 3727–3746, doi:10.1007/s00024-021-02800-4,

732   2021.

733   Ding, A. J., Huang, X., Nie, W., Sun, J. N., Kerminen, V. M., Petäjä, T., Su, H., Cheng, Y. F., Yang, X.

734   Q., Wang, M. H., Chi, X. G., Wang, J. P., Virkkula, A., Guo, W. D., Yuan, J., Wang, S. Y., Zhang, R.

735   J., Wu, Y. F., Song, Y., Zhu, T., Zilitinkevich, S., Kulmala, M. and Fu, C. B.: Enhanced haze pollution

736   by   black   carbon   in   megacities   in   China,   Geophys.   Res.   Lett.,   43(6),   2873–2879,

737   doi:10.1002/2016GL067745, 2016.

738   Easter, R. C., Ghan, S. J., Zhang, Y., Saylor, R. D., Chapman, E. G., Laulainen, N. S., Abdul-Razzak,

739   H., Leung, L. R., Bian, X. and Zaveri, R. A.: MIRAGE: Model description and evaluation of aerosols

740   and trace gases, J. Geophys. Res. D Atmos., 109(20), doi:10.1029/2004JD004571, 2004.

741   Emmons, L. K., Walters, S., Hess, P. G., Lamarque, J. F., Pfister, G. G., Fillmore, D., Granier, C.,

742   Guenther, A., Kinnison, D., Laepple, T., Orlando, J., Tie, X., Tyndall, G., Wiedinmyer, C., Baughcum,

743   S. L. and Kloster, S.: Description and evaluation of the Model for Ozone and Related chemical Tracers,

744   version 4 (MOZART-4), Geosci. Model Dev., 3(1), 43–67, doi:10.5194/gmd-3-43-2010, 2010.

745   Emmons, L. K., Schwantes, R. H., Orlando, J. J., Tyndall, G., Kinnison, D., Lamarque, J. F., Marsh, D.,

746   Mills, M. J., Tilmes, S., Bardeen, C., Buchholz, R. R., Conley, A., Gettelman, A., Garcia, R., Simpson,

747   I., Blake, D. R., Meinardi, S. and Pétron, G.: The Chemistry Mechanism in the Community Earth System

748   Model Version 2 (CESM2), J. Adv. Model. Earth Syst., 12(4), 1–21, doi:10.1029/2019MS001882,

749   2020.

750   Fahey, K. M. and Pandis, S. N.: Optimizing model performance: variable size resolution in cloud

751   chemistry modeling, Atmos. Environ., 35(26), 4471–4478, doi:https://doi.org/10.1016/S1352-

752   2310(01)00224-2, 2001.

753   Fast, J. D., Gustafson Jr, W. I., Easter, R. C., Zaveri, R. A., Barnard, J. C., Chapman, E. G., Grell, G.

754   A. and Peckham, S. E.: Evolution of ozone, particulates, and aerosol direct forcing in an urban area

755   using a new fully-coupled meteorology, chemistry, and aerosol model, J. Geophys. Res, 111(5),

756   D21305, 2006.

757   Gautam, R., Hsu, N. C., Kafatos, M. and Tsay, S.: Influences of winter haze on fog / low cloud over the

758   Indo-Gangetic plains, , 112(June 2006), 1–11, doi:10.1029/2005JD007036, 2007.

759   Ghude, S. D., Kulkarni, S. H., Jena, C., Pfister, G. G., Beig, G., Fadnavis, S. and Van Der, R. J.:
760   Application of satellite observations for identifying regions of dominant sources of nitrogen oxides over
761   the indian subcontinent, J. Geophys. Res. Atmos., 118(2), 1075–1089, doi:10.1029/2012JD017811,
762   2013.

763   Ghude, S. D., Chate, D. M., Jena, C., Beig, G., Kumar, R., Barth, M. C., Pfister, G. G., Fadnavis, S. and
764   Pithani, P.: Premature mortality in India due to PM2.5 and ozone exposure, Geophys. Res. Lett., 43(9),
765   4650–4658, doi:https://doi.org/10.1002/2016GL068949, 2016.

766   Ghude, S. D., Bhat, G. S., Prabhakaran, T., Jenamani, R. K., Chate, D. M., Safai, P. D., Karipot, A. K.,
767   Konwar, M., Pithani, P., Sinha, V., Rao, P. S. P., Dixit, S. A., Tiwari, S., Todekar, K., Varpe, S.,
768   Srivastava, A. K., Bisht, D. S., Murugavel, P., Ali, K., Mina, U., Dharua, M., Jaya Rao, Y.,
769   Padmakumari, B., Hazra, A., Nigam, N., Shende, U., Lal, D. M., Chandra, B. P., Mishra, A. K., Kumar,
770   A., Hakkim, H., Pawar, H., Acharja, P., Kulkarni, R., Subharthi, C., Balaji, B., Varghese, M., Bera, S.
771   and Rajeevan, M.: Winter fog experiment over the Indo-Gangetic plains of India, Curr. Sci., 112(4),
772   767–784, doi:10.18520/cs/v112/i04/767-784, 2017.

773   Ghude, S. D., Kumar, R., Jena, C., Debnath, S., Kulkarni, R. G., Alessandrini, S., Biswas, M., Kulkrani,
774   S., Pithani, P., Kelkar, S., Sajjan, V., Chate, D. M., Soni, V. K., Singh, S., Nanjundiah, R. S. and
775   Rajeevan, M.: Evaluation of PM2.5 forecast using chemical data assimilation in the WRF-Chem model:
776   A novel initiative under the Ministry of Earth Sciences Air Quality Early Warning System for Delhi,
777   India, Curr. Sci., 118(11), 1803–1815, doi:10.18520/cs/v118/i11/1803-1815, 2020.

778   Govardhan, G., Nanjundiah, R. S., Satheesh, S. K., Krishnamoorthy, K. and Kotamarthi, V. R.:
779   Performance of WRF-chem over indian region: Comparison with measurements, J. Earth Syst. Sci.,
780   124(4), 875–896, doi:10.1007/s12040-015-0576-7, 2015.

781   Grell, G. A., Peckham, S. E., Schmitz, R., McKeen, S. A., Frost, G., Skamarock, W. C. and Eder, B.:
782   Fully coupled "online" chemistry within the WRF model, Atmos. Environ., 39(37), 6957–6975,
783   doi:https://doi.org/10.1016/j.atmosenv.2005.04.027, 2005.

784   Guenther, A., Karl, T., Harley, P., Weidinmyer, C., Palmer, P. I. and Geron, C.: Edinburgh Research
785   Explorer Estimates of global terrestrial isoprene emissions using MEGAN (Model of Emissions of
786   Gases and Aerosols from Nature) and Physics Estimates of global terrestrial isoprene emissions using
787   MEGAN (Model of Emissions of Gases an, Atmos. Chem. Phys., (6), 3181–3210, 2006.

788   Gundel, L. A., Benner, W. H. and Hansen, A. D. A.: Chemical composition of fog water and interstitial
789   aerosol in Berkeley, California, Atmos. Environ., 28(16), 2715–2725, doi:https://doi.org/10.1016/1352-
790   2310(94)90443-X, 1994.

791   Gupta, T. and Mandariya, A.: Sources of submicron aerosol during fog-dominated wintertime at

792   Kanpur, Environ. Sci. Pollut. Res., 20(8), 5615–5629, doi:10.1007/s11356-013-1580-6, 2013.

793   Hakkim, H., Sinha, V., Chandra, B. P., Kumar, A., Mishra, A. K., Sinha, B., Sharma, G., Pawar, H.,

794   Sohpaul, B., Ghude, S. D., Pithani, P., Kulkarni, R., Jenamani, R. K. and Rajeevan, M.: Volatile organic

795   compound measurements point to fog-induced biomass burning feedback to air quality in the megacity

796   of Delhi, Sci. Total Environ., 689, 295–304, doi:10.1016/j.scitotenv.2019.06.438, 2019.

797   Hong, S. Y., Noh, Y. and Dudhia, J.: A new vertical diffusion package with an explicit treatment of

798   entrainment processes, Mon. Weather Rev., 134(9), 2318–2341, doi:10.1175/MWR3199.1, 2006.

799   Jacobson, M. Z., Turco, R. P., Jensen, E. J. and Toon, O. B.: Modeling coagulation among particles of

800   different composition and size, Atmos. Environ., 28(7), 1327–1338, doi:https://doi.org/10.1016/1352-

801   2310(94)90280-1, 1994.

802   Jain, S., Sharma, S. K., Vijayan, N. and Mandal, T. K.: Seasonal characteristics of aerosols (PM2.5 and

803   PM10) and their source apportionment using PMF: A four year study over Delhi, India, Elsevier Ltd.,

804   2020.

805   Jena, C., Ghude, S., Kulkarni, R., Debnath, S., Kumar, R., Soni, V. K., Acharja, P., Kulkarni, S., Khare,

806   M., Kaginalkar, A., Chate, D., Ali, K., Nanjundiah, R. and Rajeevan, M.: Evaluating the sensitivity of

807   fine particulate matter (PM$_{2.5}$) simulations to chemical mechanism in Delhi,

808   Atmos. Chem. Phys. Discuss., (3), 1–28, 2020.

809   Jena, C., Ghude, S. D., Kumar, R., Debnath, S., Govardhan, G., Soni, V. K., Kulkarni, S. H., Beig, G.,

810   Nanjundiah, R. S. and Rajeevan, M.: Performance of high resolution (400 m) PM2.5 forecast over Delhi,

811   Sci. Rep., 11(1), 1–9, doi:10.1038/s41598-021-83467-8, 2021.

812   Jenamani, R. K.: Alarming rise in fog and pollution causing a fall in maximum temperature over Delhi,

813   Curr. Sci., 93(3), 314–322 [online] Available from: http://www.jstor.org/stable/24099461, 2007.

814   Jethva, H., Chand, D., Torres, O., Gupta, P., Lyapustin, A. and Patadia, F.: Agricultural burning and air

815   quality over northern india: A synergistic analysis using nasa's a-train satellite data and ground

816   measurements, Aerosol Air Qual. Res., 18(7), 1756–1773, doi:10.4209/aaqr.2017.12.0583, 2018.

817   Katata, G., Chino, M., Kobayashi, T., Terada, H., Ota, M., Nagai, H., Kajino, M., Draxler, R., Hort, M.

818   C., Malo, A., Torii, T. and Sanada, Y.: Detailed source term estimation of the atmospheric release for

819   the Fukushima Daiichi Nuclear Power Station accident by coupling simulations of an atmospheric

820   dispersion model with an improved deposition scheme and oceanic dispersion model, Atmos. Chem.

821   Phys., 15(2), 1029–1070, doi:10.5194/acp-15-1029-2015, 2015.

822   Kaul, D. S., Gupta, T., Tripathi, S. N., Tare, V. and Collett, J. L.: Secondary organic aerosol: A

823 comparison between foggy and nonfoggy days, Environ. Sci. Technol., 45(17), 7307–7313,
824 doi:10.1021/es201081d, 2011.

825 Kedia, S., Ramachandran, S., Holben, B. N. and Tripathi, S. N.: Quantification of aerosol type, and
826 sources of aerosols over the Indo-Gangetic Plain, Atmos. Environ., 98, 607–619,
827 doi:10.1016/j.atmosenv.2014.09.022, 2014.

828 Knote, C., Tuccella, P., Curci, G., Emmons, L., Orlando, J. J., Madronich, S., Baró, R., Jiménez-
829 Guerrero, P., Luecken, D., Hogrefe, C., Forkel, R., Werhahn, J., Hirtl, M., Pérez, J. L., San José, R.,
830 Giordano, L., Brunner, D., Yahya, K. and Zhang, Y.: Influence of the choice of gas-phase mechanism
831 on predictions of key gaseous pollutants during the AQMEII phase-2 intercomparison, Atmos. Environ.,
832 115, 553–568, doi:10.1016/j.atmosenv.2014.11.066, 2014.

833 Krishna Moorthy, K., Suresh Babu, S., Manoj, M. R. and Satheesh, S. K.: Buildup of aerosols over the
834 Indian Region, Geophys. Res. Lett., 40(5), 1011–1014, doi:10.1002/grl.50165, 2013.

835 Krishna, R. K., Panicker, A. S., Yusuf, A. M. and Ullah, B. G.: On the contribution of particulate matter
836 (PM 2.5) to direct radiative forcing over two urban environments in India, Aerosol Air Qual. Res.,
837 19(2), 399–410, doi:10.4209/aaqr.2018.04.0128, 2019.

838 Kulkarni, R., Jenamani, R. K., Pithani, P. and Konwar, M.: Loss to Aviation Economy Due to Winter
839 Fog in New Delhi during the Winter of 2011 – 2016, , 1–10, 2019.

840 Kulkarni, S. H., Ghude, S. D., Jena, C., Karumuri, R. K., Sinha, B., Sinha, V., Kumar, R., Soni, V. K.
841 and Khare, M.: How Much Does Large-Scale Crop Residue Burning Affect the Air Quality in Delhi?,
842 Environ. Sci. Technol., 54(8), 4790–4799, doi:10.1021/acs.est.0c00329, 2020.

843 Kumar, A. and Sarin, M. M.: Aerosol iron solubility in a semi-arid region: temporal trend and impact
844 of anthropogenic sources, Tellus B, 62(2), doi:10.3402/tellusb.v62i2.16519, 2010.

845 Kumar, A., Hakkim, H., Sinha, B. and Sinha, V.: Gridded 1 km × 1 km emission inventory for paddy
846 stubble burning emissions over north-west India constrained by measured emission factors of 77 VOCs
847 and district-wise crop yield data, Sci. Total Environ., 789, 148064,
848 doi:10.1016/j.scitotenv.2021.148064, 2021.

849 Kumar, M., Parmar, K. S., Kumar, D. B., Mhawish, A., Broday, D. M., Mall, R. K. and Banerjee, T.:
850 Long-term aerosol climatology over Indo-Gangetic Plain: Trend, prediction and potential source fields,
851 Atmos. Environ., 180, 37–50, doi:10.1016/j.atmosenv.2018.02.027, 2018.

852 Kumar, R., Barth, M. C., Pfister, G. G., Nair, V. S., Ghude, S. D. and Ojha, N.: What controls the
853 seasonal cycle of black carbon aerosols in India?, J. Geophys. Res. Atmos., 120(15), 7788–7812,
854 doi:https://doi.org/10.1002/2015JD023298, 2015.

855   Kumar, R., Mishra, V., Buzan, J., Kumar, R., Shindell, D. and Huber, M.: Dominant control of
856   agriculture and irrigation on urban heat island in India, Sci. Rep., 7(1), 1–11, doi:10.1038/s41598-017-
857   14213-2, 2017.

858   Kumar, R., Ghude, S. D., Biswas, M., Jena, C., Alessandrini, S., Debnath, S., Kulkarni, S., Sperati, S.,
859   Soni, V. K., Nanjundiah, R. S. and Rajeevan, M.: Enhancing Accuracy of Air Quality and Temperature
860   Forecasts During Paddy Crop Residue Burning Season in Delhi Via Chemical Data Assimilation., 2020.

861   Lalchandani, V., Kumar, V., Tobler, A., M. Thamban, N., Mishra, S., Slowik, J. G., Bhattu, D., Rai, P.,
862   Satish, R., Ganguly, D., Tiwari, S., Rastogi, N., Tiwari, S., Močnik, G., Prévôt, A. S. H. and Tripathi,
863   S. N.: Real-time characterization and source apportionment of fine particulate matter in the Delhi
864   megacity area during late winter, Sci. Total Environ., 770, doi:10.1016/j.scitotenv.2021.145324, 2021.

865   Lelieveld, J., Evans, J. S., Fnais, M., Giannadaki, D. and Pozzer, A.: The contribution of outdoor air
866   pollution sources to premature mortality on a global scale, Nature, 525(7569), 367–371,
867   doi:10.1038/nature15371, 2015.

868   Ma, Y., Brooks, S. D., Vidaurre, G., Khalizov, A. F., Wang, L. and Zhang, R.: Rapid modification of
869   cloud-nucleating ability of aerosols by biogenic emissions, Geophys. Res. Lett., 40(23), 6293–6297,
870   doi:https://doi.org/10.1002/2013GL057895, 2013.

871   Maalick, Z., Kühn, T., Korhonen, H., Kokkola, H., Laaksonen, A. and Romakkaniemi, S.: Effect of
872   aerosol concentration and absorbing aerosol on the radiation fog life cycle, Atmos. Environ., 133, 26–
873   33, doi:10.1016/j.atmosenv.2016.03.018, 2016.

874   Mandariya, A. K., Gupta, T. and Tripathi, S. N.: Effect of aqueous-phase processing on the formation
875   and evolution of organic aerosol (OA) under different stages of fog life cycles, Atmos. Environ.,
876   206(November 2018), 60–71, doi:10.1016/j.atmosenv.2019.02.047, 2019.

877   Mishra, V., Ambika, A. K., Asoka, A., Aadhar, S., Buzan, J., Kumar, R. and Huber, M.: Moist heat
878   stress extremes in India enhanced by irrigation, Nat. Geosci., 13(11), 722–728, doi:10.1038/s41561-
879   020-00650-8, 2020.

880   Moore, R. H., Cerully, K., Bahreini, R., Brock, C. A., Middlebrook, A. M. and Nenes, A.:
881   Hygroscopicity and composition of California CCN during summer 2010, J. Geophys. Res. Atmos.,
882   117(7), 1–14, doi:10.1029/2011JD017352, 2012.

883   Neu, J. L. and Prather, M. J.: Toward a more physical representation of precipitation scavenging in
884   global chemistry models: Cloud overlap and ice physics and their impact on tropospheric ozone, Atmos.
885   Chem. Phys., 12(7), 3289–3310, doi:10.5194/acp-12-3289-2012, 2012.

886   Ojha, N., Sharma, A., Kumar, M., Girach, I., Ansari, T. U., Sharma, S. K., Singh, N., Pozzer, A. and

887   Gunthe, S. S.: On the widespread enhancement in fine particulate matter across the Indo-Gangetic Plain
888   towards winter, Sci. Rep., 10(1), 1–9, doi:10.1038/s41598-020-62710-8, 2020.

889   Pan, X., Chin, M., Gautam, R., Bian, H., Kim, D., Colarco, P. R., Diehl, T. L., Takemura, T., Pozzoli,
890   L., Tsigaridis, K., Bauer, S. and Bellouin, N.: A multi-model evaluation of aerosols over South Asia:
891   Common problems and possible causes, Atmos. Chem. Phys., 15(10), 5903–5928, doi:10.5194/acp-15-
892   5903-2015, 2015.

893   Pant, P., Shukla, A., Kohl, S. D., Chow, J. C., Watson, J. G. and Harrison, R. M.: Characterization of
894   ambient PM2.5 at a pollution hotspot in New Delhi, India and inference of sources, Atmos. Environ.,
895   109, 178–189, doi:10.1016/j.atmosenv.2015.02.074, 2015.

896   Patil, R. S., Kumar, R., Menon, R., Shah, M. K. and Sethi, V.: Development of particulate matter
897   speciation profiles for major sources in six cities in India, Atmos. Res., 132–133, 1–11,
898   doi:10.1016/j.atmosres.2013.04.012, 2013.

899   Pawar, H. and Sinha, B.: Residential heating emissions (can) exceed paddy-residue burning emissions
900   in   rural   northwest   India,   Atmos.   Environ.,   269,   118846,
901   doi:https://doi.org/10.1016/j.atmosenv.2021.118846, 2022.

902   Pithani, P., Ghude, S. D., Chennu, V. N., Kulkarni, R. G., Steeneveld, G. J., Sharma, A., Prabhakaran,
903   T., Chate, D. M., Gultepe, I., Jenamani, R. K. and Madhavan, R.: WRF Model Prediction of a Dense
904   Fog Event Occurred During the Winter Fog Experiment (WIFEX), Pure Appl. Geophys., 176(4), 1827–
905   1846, doi:10.1007/s00024-018-2053-0, 2019.

906   Pithani, P., Ghude, S. D., Jenamani, R. K., Biswas, M., Naidu, C. V., Debnath, S., Kulkarni, R.,
907   Dhangar, N. G., Jena, C., Hazra, A., Phani, R., Mukhopadhyay, P., Prabhakaran, T., Nanjundiah, R. S.
908   and Rajeevan, M.: Real-time forecast of dense fog events over Delhi: The performance of the wrf model
909   during the wifex field campaign, Weather Forecast., 35(2), 739–756, doi:10.1175/WAF-D-19-0104.1,
910   2020.

911   Pleim, J. E.: A combined local and nonlocal closure model for the atmospheric boundary layer. Part I:
912   Model   description   and   testing,   J.   Appl.   Meteorol.   Climatol.,   46(9),   1383–1395,
913   doi:10.1175/JAM2539.1, 2007a.

914   Pleim, J. E.: A combined local and nonlocal closure model for the atmospheric boundary layer. Part II:
915   Application and evaluation in a mesoscale meteorological model, J. Appl. Meteorol. Climatol., 46(9),
916   1396–1409, doi:10.1175/JAM2534.1, 2007b.

917   Pleim, J. E. and Chang, J. S.: A non-local closure model for vertical mixing in the convective boundary
918   layer, Atmos. Environ. Part A. Gen. Top., 26(6), 965–981, doi:https://doi.org/10.1016/0960-
919   1686(92)90028-J, 1992.

Powers, J. G., Klemp, J. B., Skamarock, W. C., Davis, C. A., Dudhia, J., Gill, D. O., Coen, J. L., Gochis, D. J., Ahmadov, R., Peckham, S. E., Grell, G. A., Michalakes, J., Trahan, S., Benjamin, S. G., Alexander, C. R., Dimego, G. J., Wang, W., Schwartz, C. S., Romine, G. S., Liu, Z., Snyder, C., Chen, F., Barlage, M. J., Yu, W. and Duda, M. G.: The weather research and forecasting model: Overview, system efforts, and future directions, Bull. Am. Meteorol. Soc., 98(8), 1717–1737, doi:10.1175/BAMS-D-15-00308.1, 2017.

Pye, H. O. T., Nenes, A., Alexander, B., Ault, A. P., Barth, M. C., Clegg, S. L., Collett, J. L., Fahey, K. M., Hennigan, C. J., Herrmann, H., Kanakidou, M., Kelly, J. T., Ku, I. T., Faye McNeill, V., Riemer, N., Schaefer, T., Shi, G., Tilgner, A., Walker, J. T., Wang, T., Weber, R., Xing, J., Zaveri, R. A. and Zuend, A.: The acidity of atmospheric particles and clouds., 2020.

Ram, K., Sarin, M. M., Sudheer, A. K. and Rengarajan, R.: Carbonaceous and secondary inorganic aerosols during wintertime fog and haze over urban sites in the Indo-Gangetic plain, Aerosol Air Qual. Res., 12(3), 355–366, doi:10.4209/aaqr.2011.07.0105, 2012.

Ram, K., Tripathi, S. N., Sarin, M. M. and Bhattu, D.: Primary and secondary aerosols from an urban site (Kanpur) in the Indo-Gangetic Plain: Impact on CCN, CN concentrations and optical properties, Atmos. Environ., 89, 655–663, doi:10.1016/j.atmosenv.2014.02.009, 2014.

Ramachandran, S., Rupakheti, M. and Lawrence, M. G.: Aerosol-induced atmospheric heating rate decreases over South and East Asia as a result of changing content and composition, Sci. Rep., 10(1), 1–17, doi:10.1038/s41598-020-76936-z, 2020.

Rengarajan, R., Sarin, M. M. and Sudheer, A. K.: Carbonaceous and inorganic species in atmospheric aerosols during wintertime over urban and high-altitude sites in North India, J. Geophys. Res. Atmos., 112(21), 1–16, doi:10.1029/2006JD008150, 2007.

Ruan, X., Zhao, C., Zaveri, R. A., He, P., Wang, X., Shao, J. and Geng, L.: Simulations of aerosol pH in China using WRF-Chem (v4 . 0): sensitivities of aerosol pH and its temporal variations during haze episodes, , 6143–6164, 2022.

Safai, P. D., Ghude, S., Pithani, P., Varpe, S., Kulkarni, R., Todekar, K., Tiwari, S., Chate, D. M., Prabhakaran, T., Jenamani, R. K. and Rajeevan, M. N.: Two-way relationship between aerosols and fog: A case study at IGI airport, New Delhi, Aerosol Air Qual. Res., 19(1), 71–79, doi:10.4209/aaqr.2017.11.0542, 2019.

Sarkar, C., Roy, A., Chatterjee, A., Ghosh, S. K. and Raha, S.: Factors controlling the long-term (2009–2015) trend of PM2.5 and black carbon aerosols at eastern Himalaya, India, Sci. Total Environ., 656, 280–296, doi:10.1016/j.scitotenv.2018.11.367, 2019.

Sarkar, S., Chokngamwong, R., Cervone, G., Singh, R. P. and Kafatos, M.: Variability of aerosol optical

953 depth and aerosol forcing over India, Adv. Sp. Res., 37(12), 2153–2159, doi:10.1016/j.asr.2005.09.043,
954 2006.

955 Sengupta, A., Govardhan, G., Debnath, S., Yadav, P., Kulkarni, S. H., Parde, A. N., Lonkar, P.,
956 Dhangar, N., Gunwani, P., Wagh, S., Nivdange, S., Jena, C., Kumar, R. and Ghude, S. D.: Probing into
957 the wintertime meteorology and particulate matter (PM2.5 and PM10) forecast over Delhi, Atmos.
958 Pollut. Res., 13(6), 101426, doi:https://doi.org/10.1016/j.apr.2022.101426, 2022.

959 Shao, N., Lu, C., Jia, X., Wang, Y., Li, Y., Yin, Y., Zhu, B., Zhao, T., Liu, D., Niu, S., Fan, S., Yan, S.
960 and Lv, J.: Self-enhanced aerosol – fog interactions in two successive radiation fog events in the Yangtze
961 River Delta , China : A simulation study, , (January), 1–46, 2023.

962 Sharma, A. R., Kharol, S. K., Badarinath, K. V. S. and Singh, D.: Impact of agriculture crop residue
963 burning on atmospheric aerosol loading - A study over Punjab State, India, Ann. Geophys., 28(2), 367–
964 379, doi:10.5194/angeo-28-367-2010, 2010.

965 Sharma, G., Annadate, S. and Sinha, B.: Will open waste burning become India ' s largest air pollution
966 source ? ☆, Environ. Pollut., 292(PA), 118310, doi:10.1016/j.envpol.2021.118310, 2022.

967 Singh, A. and Dey, S.: Influence of aerosol composition on visibility in megacity Delhi, Atmos.
968 Environ., 62, 367–373, doi:10.1016/j.atmosenv.2012.08.048, 2012.

969 Singh, N., Banerjee, T., Raju, M. P., Deboudt, K., Sorek-Hamer, M., Singh, R. S. and Mall, R. K.:
970 Aerosol chemistry, transport, and climatic implications during extreme biomass burning emissions over
971 the Indo-Gangetic Plain, Atmos. Chem. Phys., 18(19), 14197–14215, doi:10.5194/acp-18-14197-2018,
972 2018.

973 Srivastava, P., Dey, S., Srivastava, A. K., Singh, S. and Tiwari, S.: Most probable mixing state of
974 aerosols in Delhi NCR, northern India, Atmos. Res., 200(September 2017), 88–96,
975 doi:10.1016/j.atmosres.2017.09.018, 2018.

976 Steeneveld, G. J., Ronda, R. J. and Holtslag, A. A. M.: The Challenge of Forecasting the Onset and
977 Development of Radiation Fog Using Mesoscale Atmospheric Models, Boundary-Layer Meteorol.,
978 154(2), 265–289, doi:10.1007/s10546-014-9973-8, 2015.

979 Stolaki, S., Haeffelin, M., Lac, C., Dupont, J. C., Elias, T. and Masson, V.: Influence of aerosols on the
980 life cycle of a radiation fog event. A numerical and observational study, Atmos. Res., 151, 146–161,
981 doi:10.1016/j.atmosres.2014.04.013, 2015.

982 Syed, F. S., Körnich, H. and Tjernström, M.: On the fog variability over south Asia, Clim. Dyn., 39(12),
983 2993–3005, doi:10.1007/s00382-012-1414-0, 2012.

984 Tare, V., Tripathi, S. N., Chinnam, N., Srivastava, A. K., Dey, S., Manar, M., Kanawade, V. P.,

985   Agarwal, A., Kishore, S., Lal, R. B. and Sharma, M.: Measurements of atmospheric parameters during
986   Indian Space Research Organization Geosphere Biosphere Program Land Campaign II at a typical
987   location in the Ganga basin: 2. Chemical properties, J. Geophys. Res. Atmos., 111(23),
988   doi:10.1029/2006JD007279, 2006.

989   Tav, J., Masson, O., Burnet, F., Paulat, P., Bourrianne, T., Conil, S. and Pourcelot, L.: Determination
990   of fog-droplet deposition velocity from a simple weighing method, Aerosol Air Qual. Res., 18(1), 103–
991   113, doi:10.4209/aaqr.2016.11.0519, 2018.

992   Taylor, K. E.: in a Single Diagram, , 106, 7183–7192, 2001.

993   Van Der Velde, I. R., Steeneveld, G. J., Wichers Schreur, B. G. J. and Holtslag, A. A. M.: Modeling
994   and forecasting the onset and duration of severe radiation fog under frost conditions, Mon. Weather
995   Rev., 138(11), 4237–4253, doi:10.1175/2010MWR3427.1, 2010.

996   Verma, S., Ramana, M. V. and Kumar, R.: Atmospheric rivers fueling the intensification of fog and
997   haze over Indo-Gangetic Plains, Sci. Rep., 12(1), 1–9, doi:10.1038/s41598-022-09206-9, 2022.

998   Wang, T., Liu, M., Liu, M., Song, Y., Xu, Z., Shang, F., Huang, X., Liao, W., Wang, W., Ge, M., Cao,
999   J., Hu, J., Tang, G., Pan, Y., Hu, M. and Zhu, T.: Sulfate Formation Apportionment during Winter Haze
1000   Events in North China, Environ. Sci. Technol., 56(12), 7771–7778, doi:10.1021/acs.est.2c02533, 2022.

1001   Wexler, A. S., Lurmann, F. W. and Seinfeld, J. H.: Modelling urban and regional aerosols—I. model
1002   development, Atmos. Environ., 28(3), 531–546, doi:https://doi.org/10.1016/1352-2310(94)90129-5,
1003   1994.

1004   Wiedinmyer, C., Akagi, S. K., Yokelson, R. J., Emmons, L. K., Al-Saadi, J. A., Orlando, J. J. and Soja,
1005   A. J.: The Fire INventory from NCAR (FINN): A high resolution global model to estimate the emissions
1006   from open burning, Geosci. Model Dev., 4(3), 625–641, doi:10.5194/gmd-4-625-2011, 2011.

1007   Xiu, A. and Pleim, J. E.: Development of a land surface model. Part I: Application in a mesoscale
1008   meteorological   model,   J.   Appl.   Meteorol.,   40(2),   192–209,   doi:10.1175/1520-
1009   0450(2001)040<0192:DOALSM>2.0.CO;2, 2001.

1010   Yadav, P., Parde, A. N., Dhangar, N. G., Govardhan, G., Lal, D. M., Wagh, S., Prasad, D. S. V. V. D.,
1011   Ahmed, R. and Ghude, S. D.: Understanding the genesis of a dense fog event over Delhi using
1012   observations and high-resolution model experiments, Model. Earth Syst. Environ., doi:10.1007/s40808-
1013   022-01463-x, 2022.

1014   Yadav, R., Bhatti, M. S., Kansal, S. K., Das, L., Gilhotra, V., Sugha, A., Hingmire, D., Yadav, S.,
1015   Tandon, A., Bhatti, R., Goel, A. and Mandal, T. K.: Comparison of ambient air pollution levels of
1016   Amritsar during foggy conditions with that of five major north Indian cities: multivariate analysis and

1017   air mass back trajectories, SN Appl. Sci., 2(11), 1–11, doi:10.1007/s42452-020-03569-2, 2020.

1018   Yu, H., Liu, S. C. and Dickinson, R. E.: Radiative effects of aerosols on the evolution of the atmospheric

1019   boundary layer, J. Geophys. Res. Atmos., 107(12), doi:10.1029/2001jd000754, 2002.

1020   Zaveri, R. A., Easter, R. C. and Peters, L. K.: A computationally efficient Multicomponent Equilibrium

1021   Solver for Aerosols (MESA), J. Geophys. Res. Atmos., 110(24), 1–22, doi:10.1029/2004JD005618,

1022   2005.

1023   Zaveri, R. A., Easter, R. C., Fast, J. D. and Peters, L. K.: Model for Simulating Aerosol Interactions and

1024   Chemistry (MOSAIC), J. Geophys. Res. Atmos., 113(13), 1–29, doi:10.1029/2007JD008782, 2008.

1025   Zhang, D. and Anthes, R. A.: A High-Resolution Model of the Planetary Boundary Layer—Sensitivity

1026   Tests and Comparisons with SESAME-79 Data, J. Appl. Meteorol. Climatol., 21(11), 1594–1609,

1027   doi:10.1175/1520-0450(1982)021<1594:AHRMOT>2.0.CO;2, 1982.

1028   Zhang, F., Li, Y., Li, Z., Sun, L., Li, R., Zhao, C., Wang, P., Sun, Y., Liu, X., Li, J., Li, P., Ren, G. and

1029   Fan, T.: Aerosol hygroscopicity and cloud condensation nuclei activity during the AC3Exp campaign:

1030   Implications for cloud condensation nuclei parameterization, Atmos. Chem. Phys., 14(24), 13423–

1031   13437, doi:10.5194/acp-14-13423-2014, 2014a.

1032   Zhang, X., Musson-Genon, L., Dupont, E., Milliez, M. and Carissimo, B.: On the Influence of a Simple

1033   Microphysics Parametrization on Radiation Fog Modelling: A Case Study During ParisFog, Boundary-

1034   Layer Meteorol., 151(2), 293–315, doi:10.1007/s10546-013-9894-y, 2014b.

1035

1036

1037

1038

1039

1040

1041

1042

1043

1044

1045

1046

1047

1048

1049

1050 Table 1 Experiment set-up for the study. Numbers in parentheses for the physics options denote the

1051 namelist settings of the WRF-Chem model.

1052

	EXP 1	EXP 2	EXP 3
Meteorology Initial /lateral boundary Condition:	*NCEP Final Analysis (GFS-FNL), 1° x1°, 6 hourly*	*ERA-Interim Project, 1.125° x 0.703°, 6 hourly*	*ERA-Interim Project, 1.125° x 0.703°, 6 hourly*
Physics Options			
Cloud Physics	*Morrison 2-mom (10)*	*Morrison 2- mom (10)*	*Morrison 2- mom (10)*
Longwave Radiation	*RRTMG scheme (4)*	*RRTMG scheme (4)*	*RRTMG scheme (4)*
Shortwave Radiation	*Goddard shortwave (2)*	*RRTMG scheme (4)*	*RRTMG scheme (4)*
Surface Layer Physics	*Revised MM5 Monin-Obukhov scheme (1)*	*Revised MM5 Monin-Obukhov scheme (1)*	*Pleim-Xiu (7)*
Surface Model	*unified Noah land-surface model (2)*	*NoahMP (4)*	*Pleim-Xiu (7)*
PBL Scheme	*YSU scheme (1)*	*YSU (1)*	*ACM2 (7)*
Convective Parameterization	*Grell-Freitas (3)*	*Grell-Freitas (3)*	*Grell-Freitas (3)*
	Continuous simulation	**Meteorology refreshed every 24 hr*	***Continuous simulation: Soil nudging included*

1053

1054
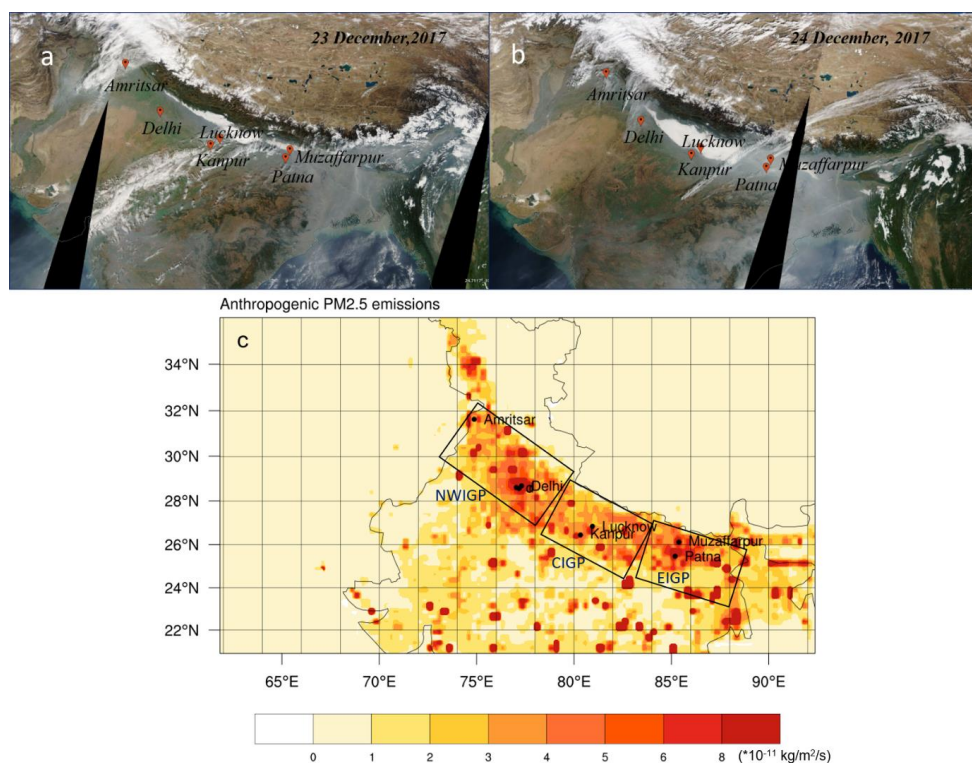
Figure 1 The MODIS reflectance (true color) map over Indo Gangetic Plains, India (study region) showing fog and haze cover on 23rd December (a) and 24th December (b)2017. (c) Anthropogenic emission of PM$_{2.5}$ over IGP for December 2017 obtained from EDGAR-HTAP. The boxes represent the regions Northwest IGP (NWIGP), Central IGP (CIGP), and East IGP (EIGP).

1062
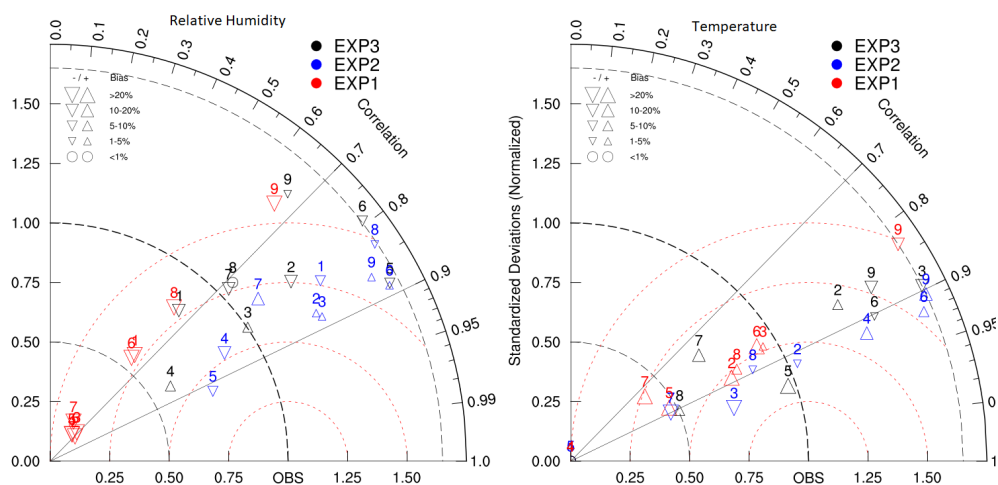
Figure 2 Taylor Diagram of simulated (WRF-Chem) and observed (CPCB) relative humidity (left) and

2-m temperature (right) over IGP. The colors indicate the experiments. The marker (triangles) size

varies with a mean bias between the experiments and observation. Upside-down triangles represent

positive bias (exp-obs) and vice versa. The stations over IGP are denoted by number 1. Amritsar, 2.

IGI Airport (Delhi), 3. IHBAS (Delhi), 4. Dwarka (Delhi), 5. RKP (Delhi), 6. Kanpur, 7. Lucknow, 8.

Patna, 9. Muzaffarpur. The locations are marked in Fig.1a.

1069
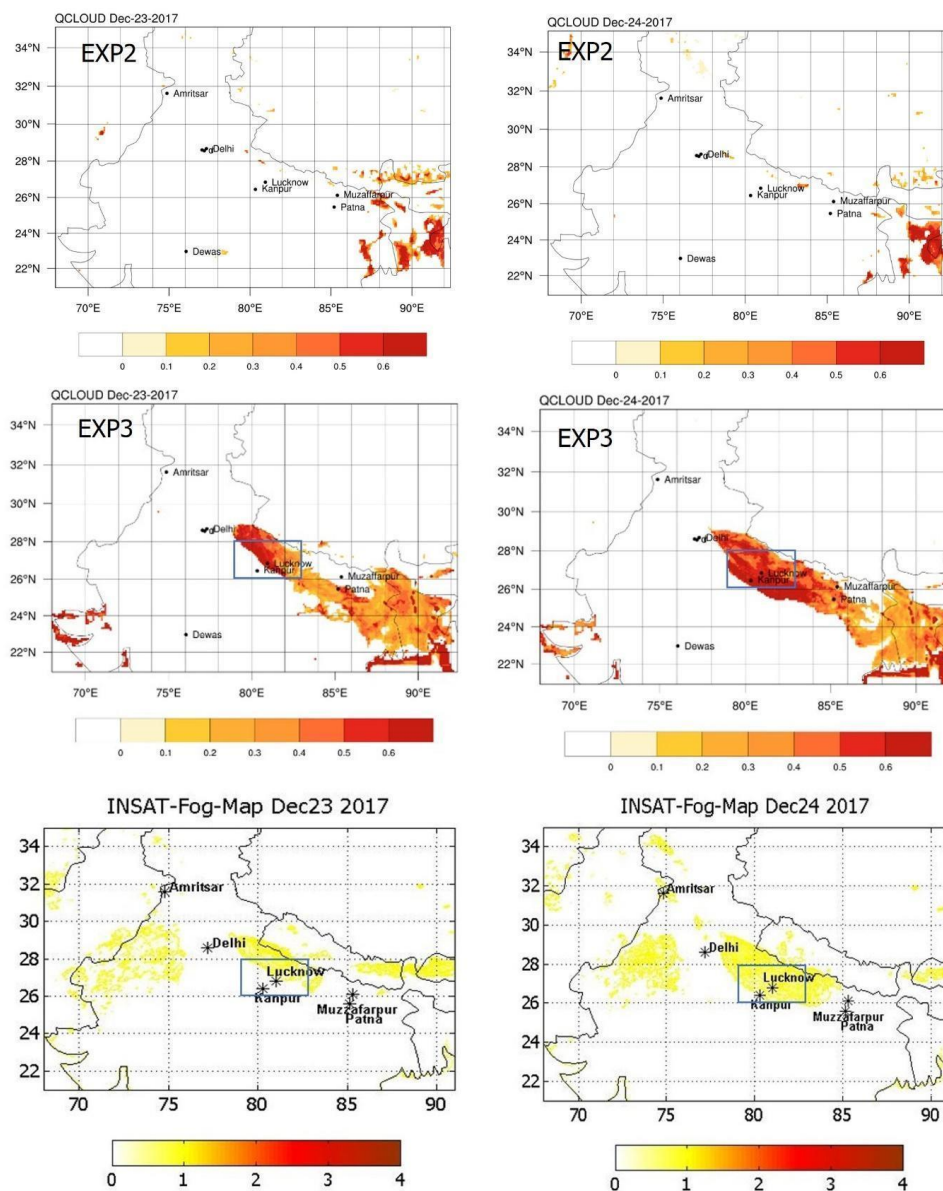
1070

1071   Figure 3 Comparison of fog coverage from WRF-Chem and INSAT-3D satellite for 23 and 24 Dec

1072   2017. WRF-Chem fog is represented by surface layer cloud water mixing ratios (in g m^{-3}) whereas

1073   INSAT-3D provides fog intensity which varies from 0 to 4 indicating SHALLOW, MODERATE,

1074   DENSE, and VERY_DENSE, respectively. The rectangle in central IGP is the region for the time

1075   series analysis.

1076
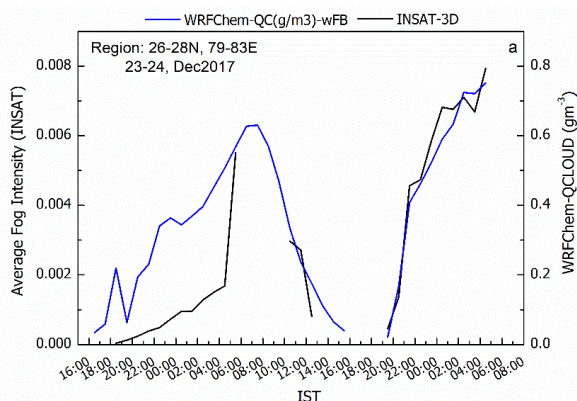
1077

1078   Figure 4 Average Hourly variation of fog on 23 and 24 December 2017 from WRF-Chem EXP3

1079   simulation and INSAT-3D satellite between 26°N-28°N,79°E-83°E (region shown in Fig 3). The time

1080   is in IST (Indian Standard Time; IST is 5.5 hours ahead of Universal Time Coordinate (UTC).

1081

1082
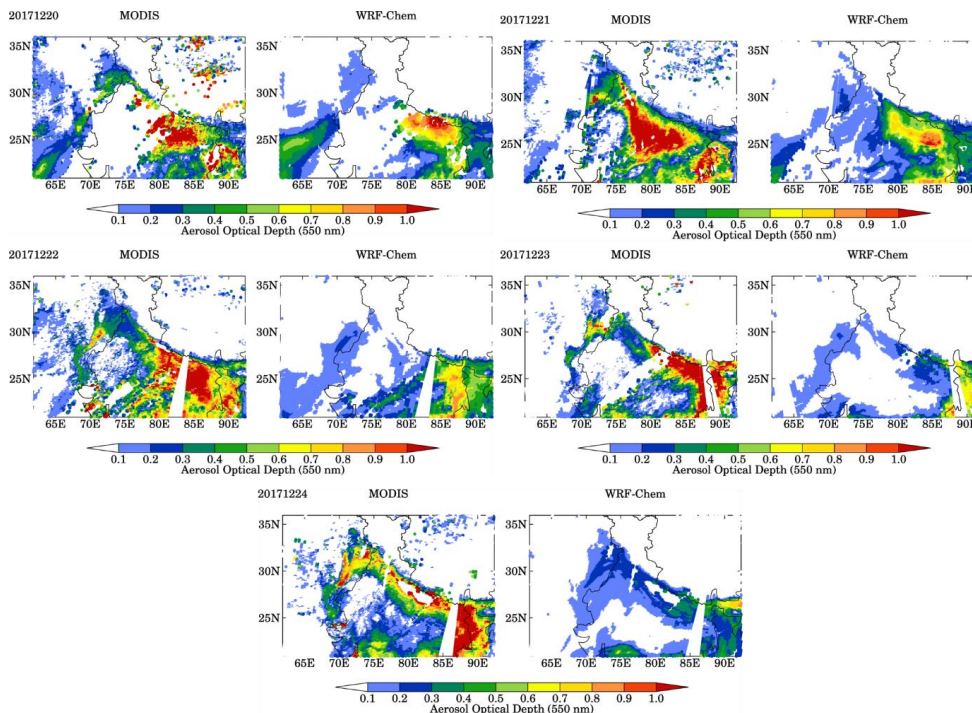
1083

1084   Figure 5 Comparison of WRF-Chem AOD with MODIS observation over the model domain on 20,
1085   21, 22, 23, and 24 December 2017.

1086

1087   .

1088
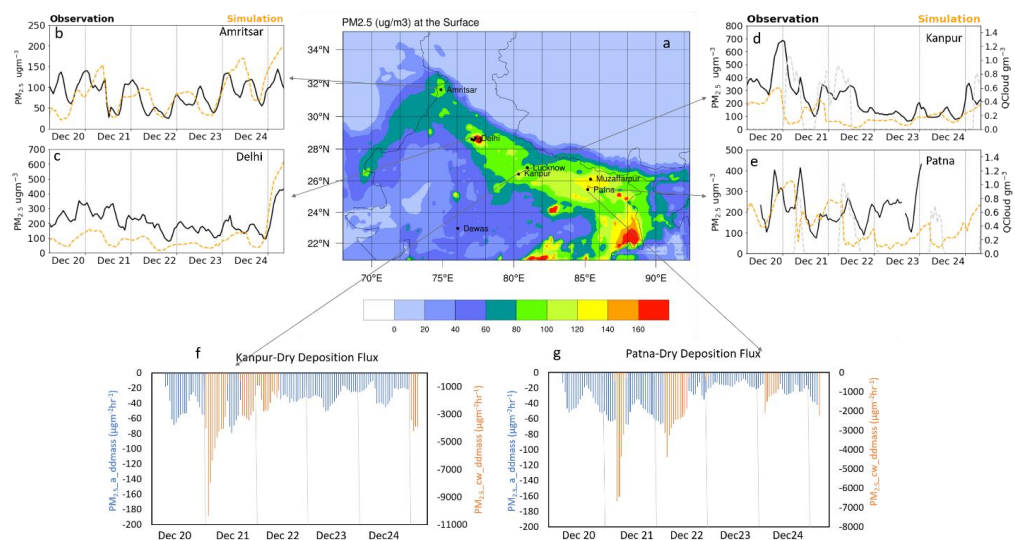
1089

1090 Figure 6 WRF-Chem simulated surface PM$_{2.5}$ map over IGP (a); comparison of WRF-Chem PM$_{2.5}$ with

1091 CPCB observation for the period 20-24Dec 2017 for (b) Amritsar, (c) Delhi, (d) Kanpur and (e) Patna.

1092 Dry Deposition rate of PM$_{2.5}$ for (f) Kanpur and (g) Patna. The grey dotted line in (d) Kanpur and (e)

1093 Patna is fog (QCloud) present during the study period.

1094
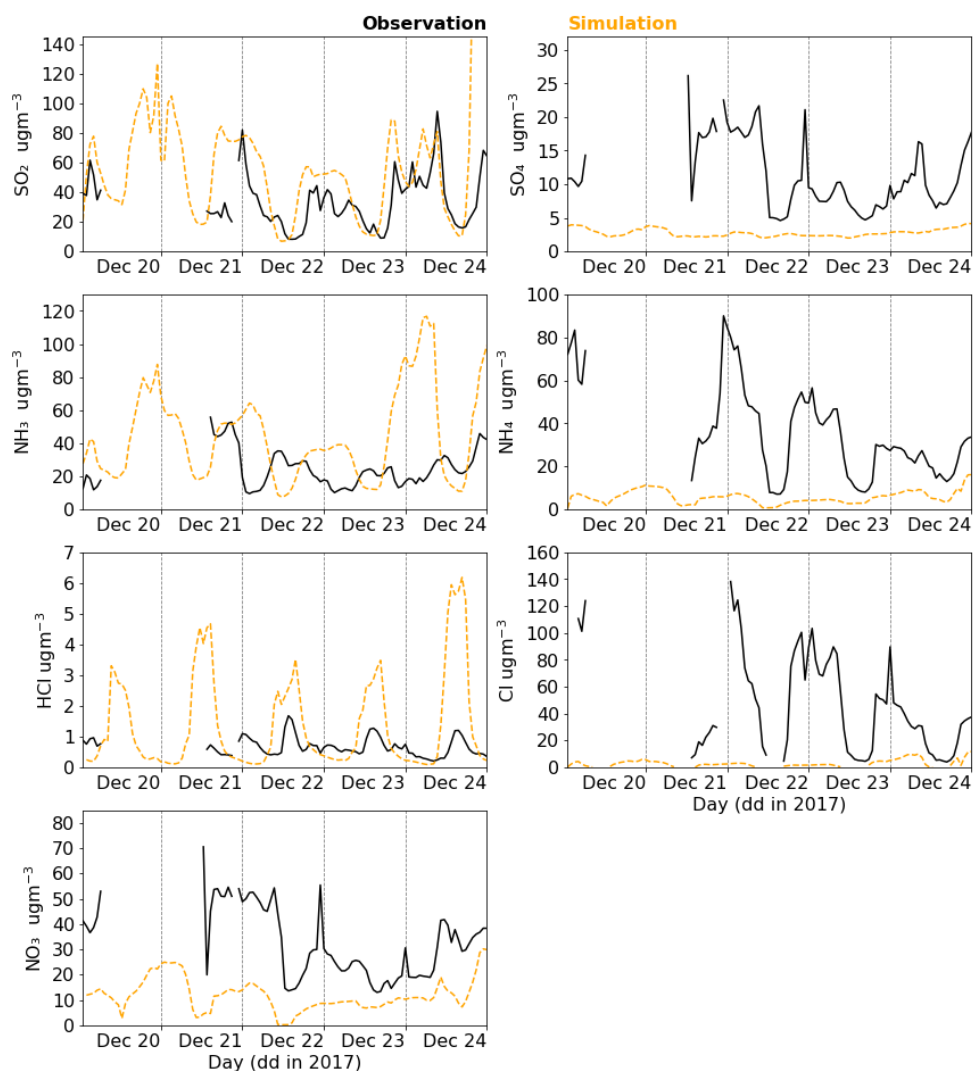
Figure 7 Comparison of WRF-Chem simulated ions (SO_4^{2-}, NH_4^+, NO_3^-, Cl^-) and trace gases (SO_2, NH_3 & HCl) with the observation from WIFEX campaign at Delhi.
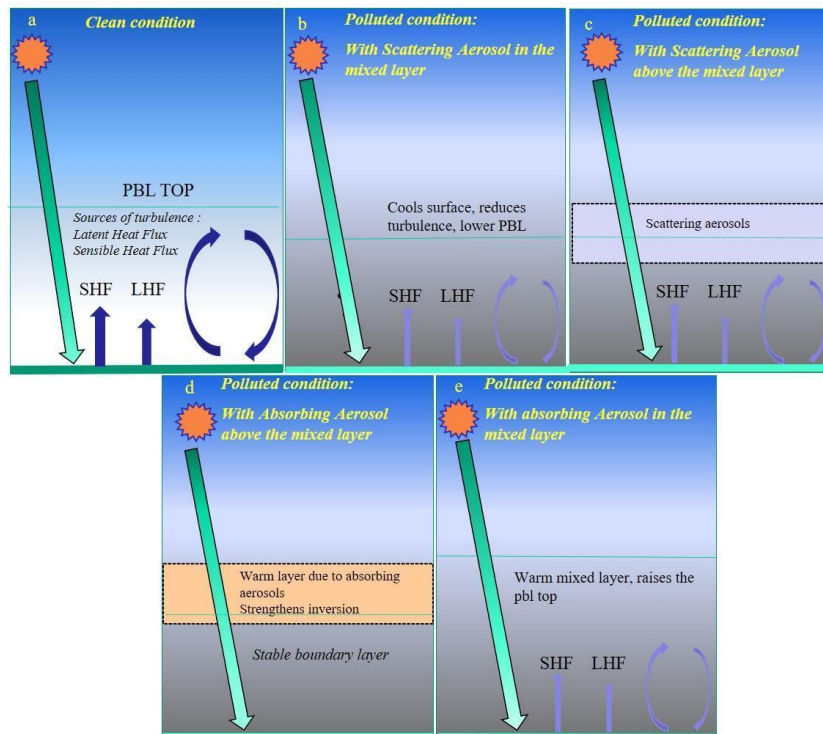
1101

1102   Figure 8 Schematic diagram of Aerosol Radiation Feedback.

1103

1104
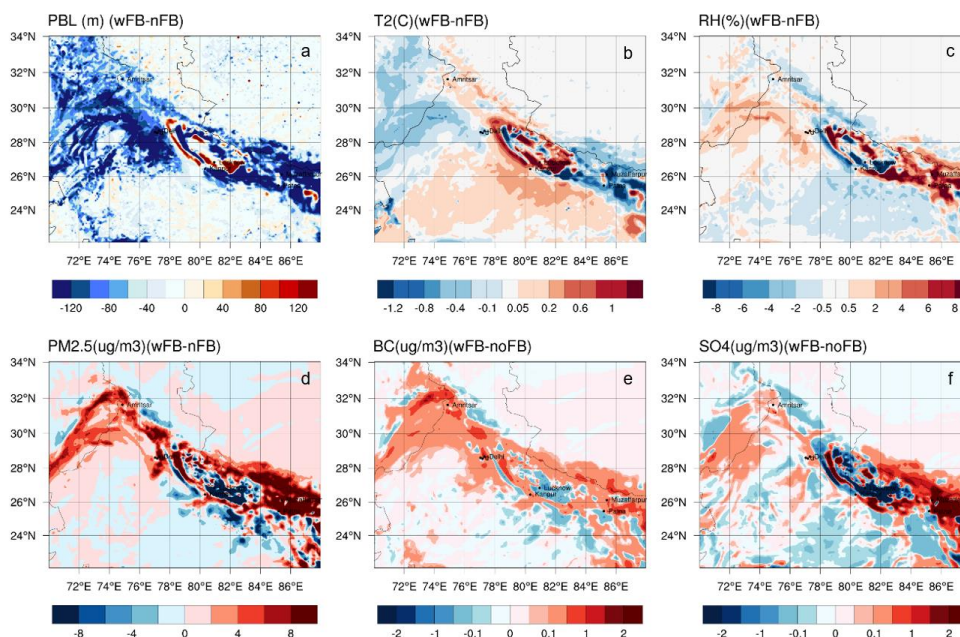
1105
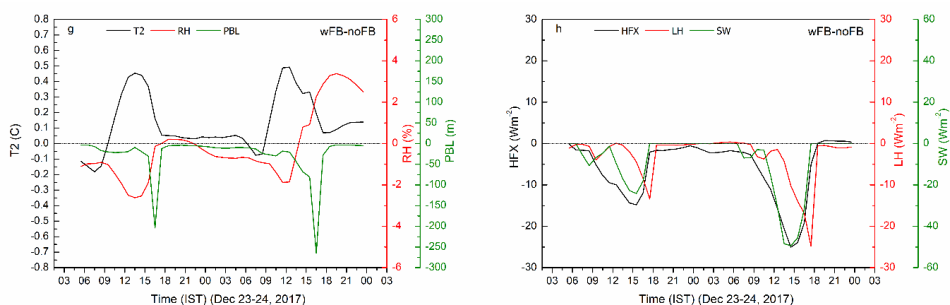
1106

Figure 9 Effect of Aerosol Radiation feedback (wFB-nFB) on (a) PBL height, (b) 2-m temperature, (c)
2-m relative humidity, (d) surface PM$_{2.5}$, (e) surface BC and (f) surface SO$_4$ for December 24 at local
noon (13:30-15:30 IST). (g) The time series of ΔPBL, ΔT2, and ΔRH; (h) ΔHFX (sensible heat flux),
ΔLH (latent heat flux), and ΔSWF (downward shortwave flux) over CIGP for December 23 and 24. Δ
denotes the difference between with and without AR feedback (wFB-nFB).

1112
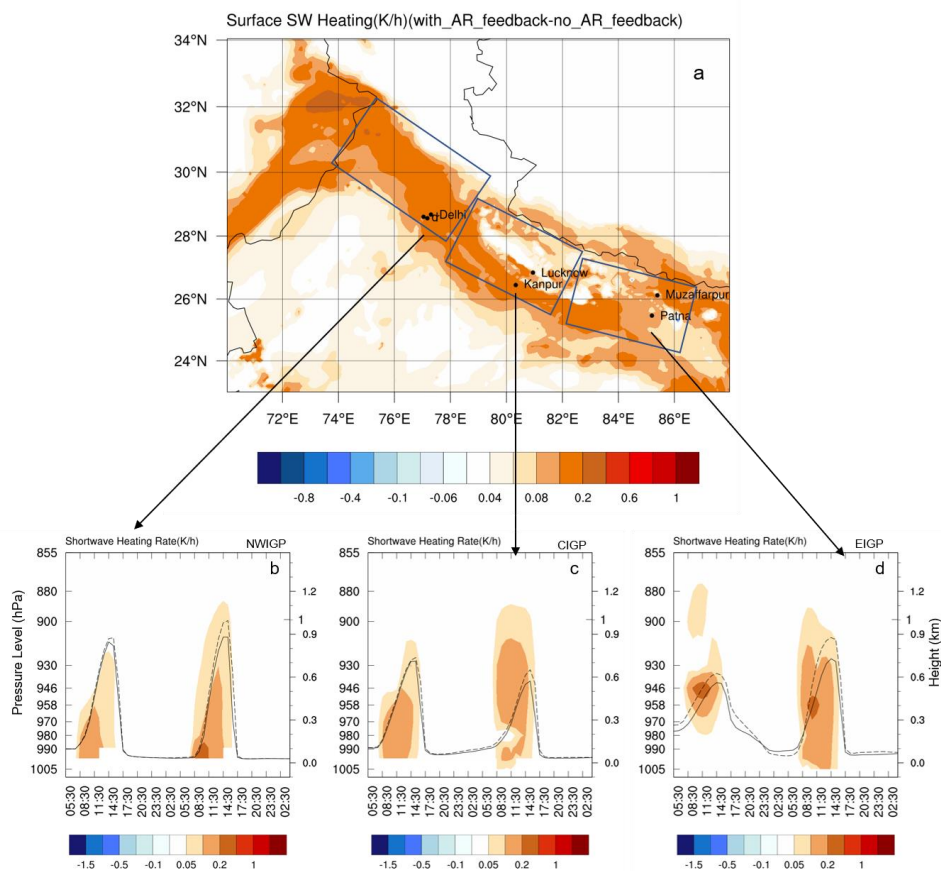
1113

Figure 10 Differences in shortwave heating rates (K h⁻¹) between simulations with and without aerosol

radiation feedback (a) at the surface, and for pressure-time cross-sections over (b) NWIGP, (c) CIGP.

And (d) EIGP for December 23 and 24. The solid and dashed lines are the PBL height with and without

AR feedback respectively. The time is in IST.
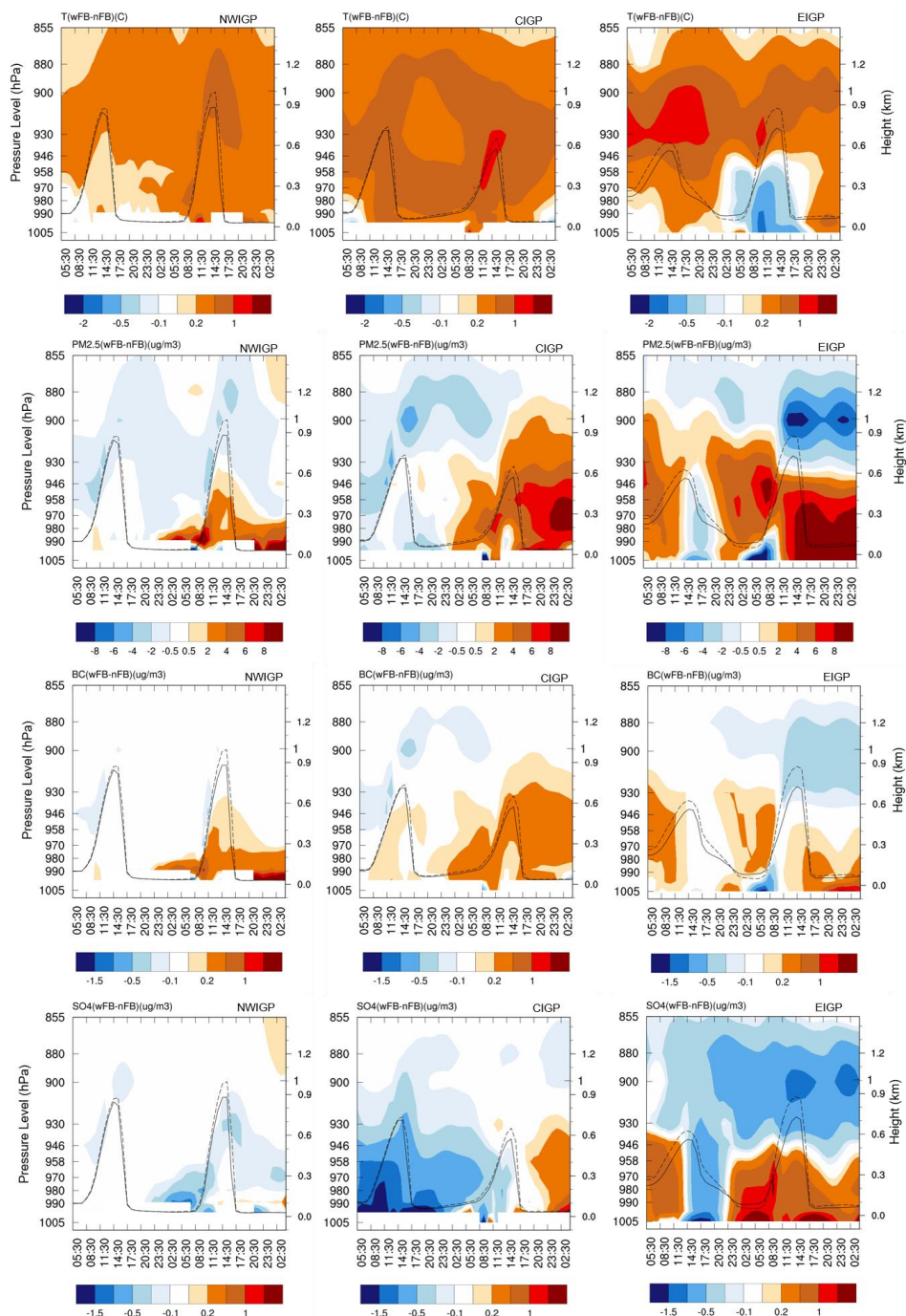
1118

1119

1120

1121 Figure 11 Pressure-time cross-section of the differences in T, $PM_{2.5}$, BC and SO_4^{2-} between simulations

1122 with and without the AR feedback for December 23 and 24. The solid and dashed lines are the PBL

1123 height with and without AR feedback respectively. The time is in IST.

1124

1125
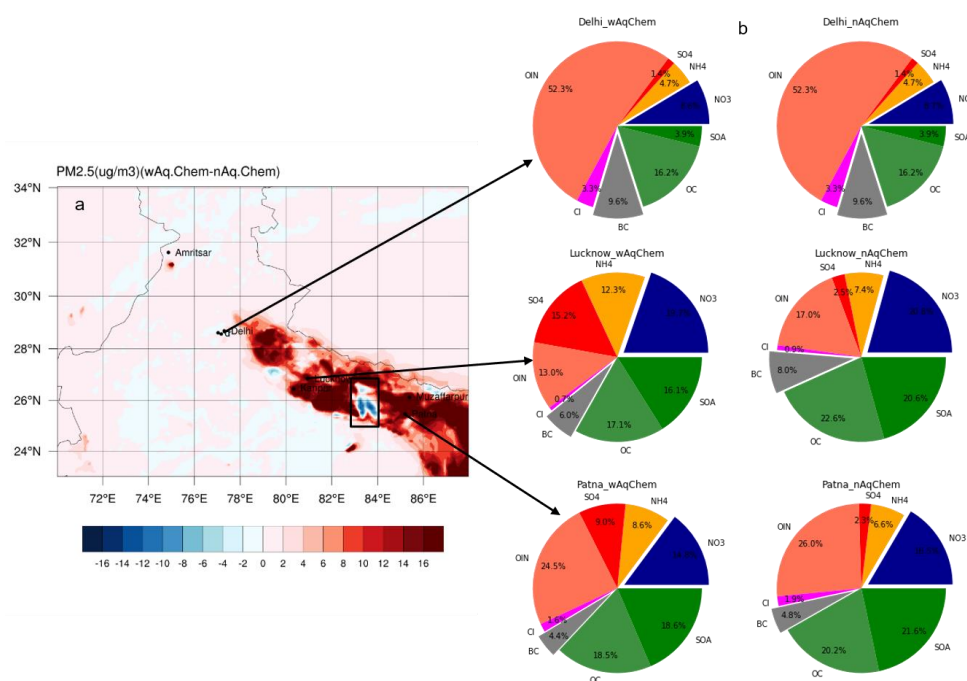
1126

1127 Figure 12 (a) Surface $\Delta PM_{2.5}$ (wAq.chem-noAq.chem) and (b) pie charts of $PM_{2.5}$ composition

1128 distribution for the two cases, with and without Aqueous phase Chemistry for 24 Dec 2017. The

1129 stations Delhi, Lucknow (LKN), and Patna are representative of NWIGP, CIGP, and EIGP regions

1130 respectively.

1131
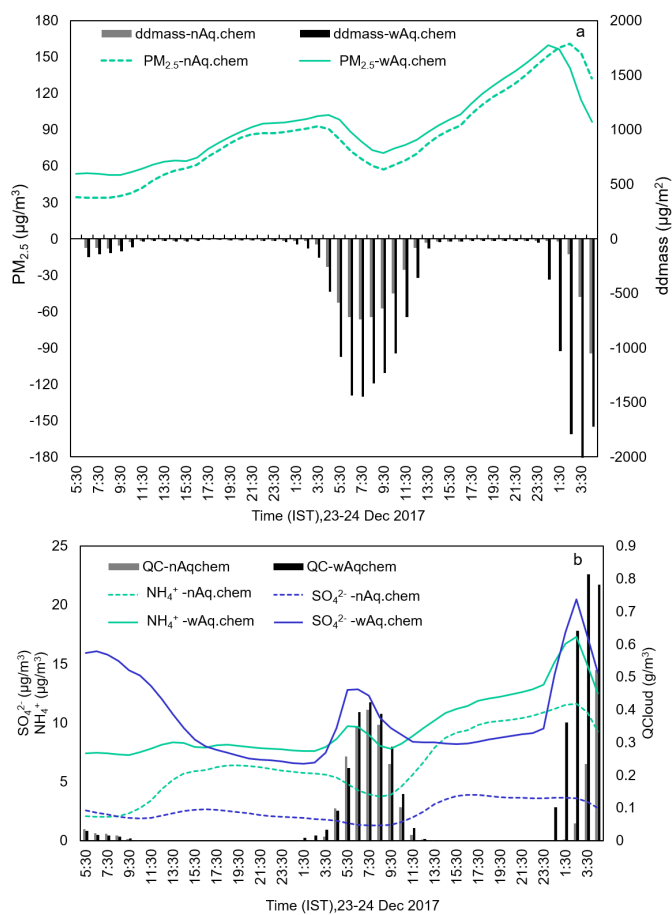
1132

1133   Figure 13 Time series of (a) PM$_{2.5}$ and its dry deposition mass concentration change (ddmass), (b)

1134   SO$_4^{2-}$, NH$_4^+$ and QCloud with and without aqueous phase chemistry included in the model,

1135   averaged over the region bounded by a black rectangle in Fig. 12.

1136

1137
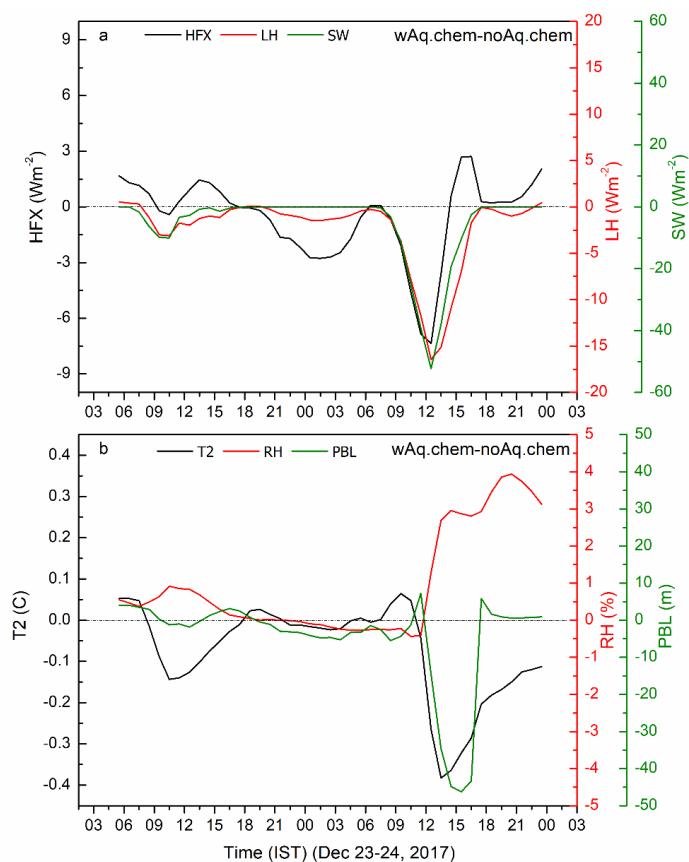
1138

1139

1140   Figure 14 Time series of (a) ΔHFX (sensible heat flux), ΔLH (latent heat flux), and ΔSWF

1141   (downward shortwave flux); (b) ΔT2, ΔRH, and ΔPBL over CIGP (79E-83E,26N-28N). Δ

1142   denotes the difference between with and without aqueous phase chemistry.

1143
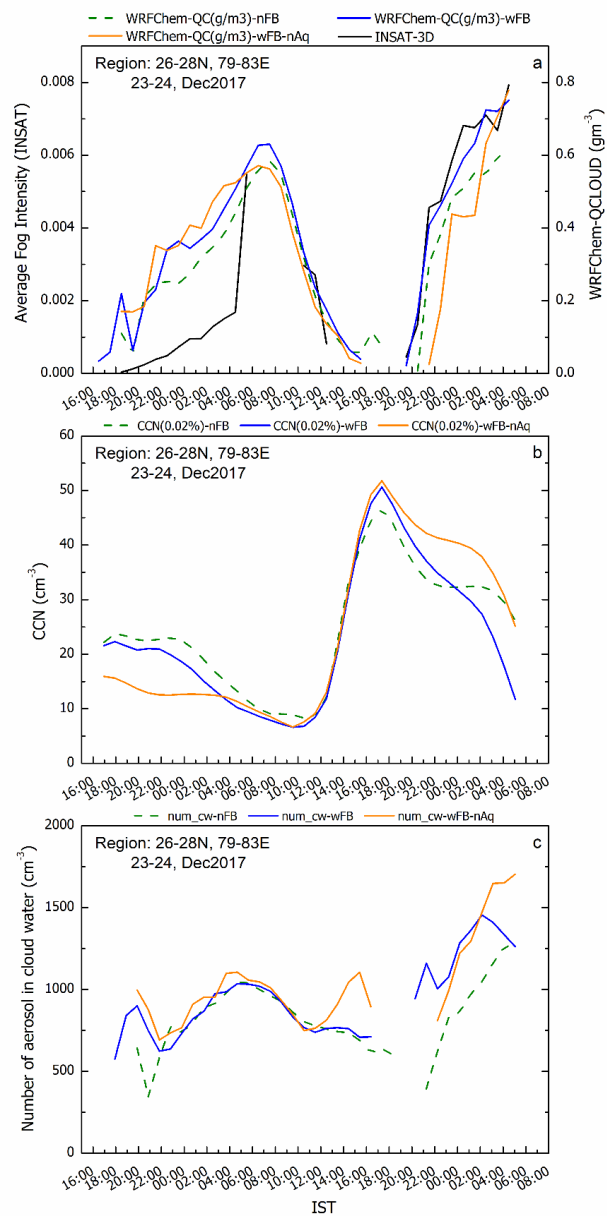
Figure 15 Hourly variation in (a) fog intensity from INSAT-3D and WRF-Chem simulated QCloud
cloud (b) WRF-Chem CCN at 0.02% supersaturation, and (c) WRF-Chem number of activated
aerosols for, with AR feedback, no AR Feedback, and no Aqueous phase chemistry experiments.
(Time in UTC)